Band alignment in Zn(1x)MgxO:Al/SiOx/Si heterostructures for photovoltaic applications realized by atomic layer deposition: Effects of Al doping and Mg alloying

Journal of Applied Physics

RESEARCH ARTICLE | DECEMBER 27 2024

Band alignment in $Zn_{(1-x)}Mg_xO$:Al/SiO_x/Si heterostructures for photovoltaic applications realized by atomic layer deposition: Effects of Al doping and Mg alloying

R. Schifano ; S. Gieraltowska ; J. Kurek ; L. Wachnicki ; U. Rehman ; D. Budiakivska ; S. Chusnutdinow ; K. Kopalko; S. Porro ; R. Jakiela ; R. Minikayev ; B. S. Witkowski ; M. Pawlowski ; C. Jastrzebski ; A. Thøgersen

J. Appl. Phys. 136, 245304 (2024)
https://doi.org/10.1063/5.0241865

Journal of Applied Physics ARTICLE pubs.aip.org/aip/jap

Band alignment in $Zn_{(1-x)}Mg_xO$:Al/SiO_x/Si heterostructures for photovoltaic applications realized by atomic layer deposition: Effects of Al doping and Mg alloying

Cite as: J. Appl. Phys. **136**, 245304 (2024); doi: 10.1063/5.0241865
Submitted: 1 October 2024 · Accepted: 6 December 2024 ·
Published Online: 27 December 2024

R. Schifano,[1,a)] S. Gieraltowska,[1] J. Kurek,[1,2,3] L. Wachnicki,[1] U. Rehman,[1] D. Budiakivska,[1,2] S. Chusnutdinow,[1] K. Kopalko,[1] S. Porro,[4] R. Jakiela,[1] R. Minikayev,[1] B. S. Witkowski,[1] M. Pawlowski,[2] C. Jastrzebski,[2] and A. Thøgersen[5]

AFFILIATIONS

[1]Institute of Physics, Polish Academy of Sciences, Al. Lotników 32/46, 02-668 Warsaw, Poland
[2]Faculty of Physics, Warsaw University of Technology, ul. Koszykowa 75, 02-662 Warsaw, Poland
[3]VIGO Photonics S.A., ul. Poznanska 129/133, 05-850 Ozarow Mazowiecki, Poland
[4]Dipartimento di Scienza Applicata e Tecnologia, Politecnico di Torino, Corso Duca degli Abruzzi 24, 10129 Torino, Italy
[5]SINTEF Industry, Materials Physics, Forskningsveien 1, 0373 Oslo, Norway

[a)]**Author to whom correspondence should be addressed:** schifano@ifpan.edu.pl

ABSTRACT

In this work, the impact of Al doping and Mg alloying on the conduction band misalignment (ΔE_C) between ZnO and (100) Si with a SiO_x interlayer was studied by combining capacitance vs voltage, Hall and x-ray diffraction measurements, energy-dispersive x-ray spectroscopy, secondary mass spectrometry, and high-resolution scanning transmission electron microscopy. To decouple the effect of the high carrier density in the ZnO-based layers due to the Al introduction, the measured ΔE_C was corrected for the conduction band lowering effect taking into account the conduction band non-parabolicity of ZnO. Then, from the Mg content dependence, using the interface-induced gap states approach, branch point energies referred to the valence band maximum equal to (2.7 ± 0.2) and (3.6 ± 0.4) eV were extracted for ZnO and MgO, respectively. These branch point energies were obtained under the assumption of a linear variation between the respective values of the corresponding two binary compound semiconductors, ZnO and MgO, and taking into account the presence of the SiO_x interlayer. Furthermore, in the case of the undoped $Zn_{0.96}Mg_{0.04}O$ layers, a ~0.27 eV reduced ΔE_C was found, with the difference with respect to $Zn_{0.94}Mg_{0.06}O$:Al attributed to the presence of a downward band bending toward the interface with SiO_x. Full 1×1 cm test solar cells based on $Zn_{0.8}Mg_{0.2}O$:Al layers exhibited short circuit currents, open circuit voltages, fill factors, and efficiencies that varied in the (28 ± 1) mA/cm^2, (430 ± 20) mV, (61 ± 2)%, and (7.2 ± 0.3)% ranges with the residual $\Delta E_C \sim 0.6$ eV being among the main causes of the reduced device performances.

I. INTRODUCTION

In the past years, promising efficiencies (ηs) equal to ~13%–15% and ~16.5% were obtained in the case of n-ITO/n-Si isotype heterostructures[1,2] and n-ITO/p-Si anisotype heterostructures,[3] respectively. These results triggered, also recently, searching for low-cost alternatives to ITO with ZnO/ZnO:Al being among the possible replacement candidates due to comparable electrical/optical properties combined with the possibility to realize Al metallizations with a specific contact resistance as low as $\sim 10^{-5}\,\Omega\,\mathrm{cm}^2$.[4,5] In addition, this device design, considering that Ag-based Ohmic contacts and ITO transparent layers for charge carrier extraction are among the current bottlenecks hindering the photovoltaic market penetration of silicon heterojunction solar cells (HJT), despite having reached a technological

maturity and efficiencies up to ∼26.8%, could be partially or in total be integrated in the current HJT solar cell structure.[6,7] This would make it possible to overcome their present reliance on Ag and In, thus resulting in an economically more affordable HJT technology also suitable for future multi-terawatt scale applications.[8] Furthermore, using a ZnO/ZnO:Al-based emitter paves the way to the utilization of technologically less demanding deposition techniques like spin-coating or spray pyrolysis for its realization, a choice that would additionally lower the present manufacturing costs. However, both n-ZnO/n-Si and n-ZnO/p-Si devices showed generally lower performances in the ∼1%–8.3% range, despite the wide variety of deposition techniques used, ranging from ultrasonic spray pyrolysis to DC magnetron sputtering on flat, texturized, and unpolished substrates.[9–13] Using nanostructured substrates,[14] the introduction of an Y_2O_3 or La_2O_3 interlayer,[15] varying the dopant, or alloying the ZnO layer[14,16,17] are routes that were also tested with ηs achieved being anyhow well below the theoretical calculation limit that is ≳20%.[18,19] In the previous listed works, little attention has been paid to the values of the ZnO/Si conduction band offset (ΔE_C), even though ΔE_C is anticipated to be one of the crucial parameters. In detail, the main impact of ΔE_C is on the open circuit voltage (V_{OC}) as well as the fill factor (FF), thus determining the devices' final η. Indeed, theoretical calculations confirm that, even for interface recombination velocities as high as $\sim 10^6$ cm s^{-1}, by turning the staggered (type II, $\Delta E_C > 0$) into a straddling (type I, $\Delta E_C < 0$) bandgap alignment, anisotype n-ZnO/p-Si based heterostructures could achieve $\eta \gtrsim 20\%$, as a consequence of a factor of ∼2 and ∼10% increase in V_{OC} and FF, respectively (see also the inset in Fig. 4 for an energy band diagram sketch).[18] Such ΔE_C tuning can be realized by alloying ZnO with Mg as shown in a previously published work.[20] However, the Mg content is practically limited to ∼2 at. %, since increasing it further produces ZnMgO films with higher resistivity that are, therefore, not suitable to act as emitters. In the present study, the route of using ∼2 at. % Al doping while increasing the Mg content up to ∼12 at. % is investigated, and a detailed analysis of the n-ZnMgO/p-Si conduction band alignment that takes into account the presence of the SiO_x interlayer is provided. It is found that by Mg alloying, ΔE_C can be reduced from ∼1 to ∼0.6 eV in the investigated range. This turns out into a ΔE_C reduction factor vs Mg content equal to ∼1.7 eV if the conduction band lowering related to the n-ZnMgO:Al high carrier concentration is taken into account. The extracted dependence is ∼1 eV lower than the value used in previous simulations, set to 2.7 eV in that case.[18] This, despite ΔE_C for the two extreme cases of ZnO and MgO vs Si being ∼0.6–0.9 eV smaller (type II) and ∼1.8 eV larger (type I) than the ones anticipated by theoretical calculations, respectively,[21–23] prevents turning the type II band alignment into a type I within the Mg alloying range in ZnO for which the wurtzite structural configuration is maintained. These findings explain the above-mentioned substantial difference between theoretically predicted and experimentally achieved ηs and point to the residual ΔE_C as one of the main causes for the low photovoltaic performances not only obtained in the test structures realized in the present work but also reported in the literature.

II. MATERIALS AND METHODS

A. Layers' growth

As substrates were used quartz, soda-lime glass and single side polished (epi-ready), commercially available boron doped p-type silicon wafers with a (100) orientation, a nominal resistivity (ρ) equal to 5–10 Ω cm, and thickness of 250 ± 10 μm bought from Siegert Wafer. An Al back contact of ∼100 nm was sputtered using a Kurt J. Lesker PVD 75 thin film deposition system on the unpolished Si wafer side. Then, the wafers were annealed for 20 min in Ar at 500 °C using a AccuThermo AW610 rapid thermal process system. Glass and quartz substrates were cleaned in 2-propanol with an ultrasonic cleaner and dipped in de-ionized water (DI). Then, all the substrates were transferred into an atomic layer deposition (ALD) reactor Savannah 100 (Veeco). The $Zn_{(1-x)}Mg_xO$ and $Zn_{(1-x)}Mg_xO$:Al layers were grown at 280 °C, if not differently stated, using diethylzinc (DEZ), de-ionized water (DI), bis(methylcyclopentadienyl)magnesium (MCp2Mg), and trimethylaluminum (TMA) as zinc, oxygen, magnesium, and aluminum precursors with pulsing times in the 0.02–0.7 s range, depending on the precursor. N_2 was used as the inert gas with 4 s long purging times after each precursor pulse. The number of cycles was adjusted to obtain films with a thickness of ∼400 nm. The recipe represents a variation from the one used in previous studies (see, e.g., Ref. 20). The first TMA pulse was introduced after a total number of DEZ +DI and MCp2Mg+DI pulses varying in the 13–24 range, if not differently stated. Subsequently, on top of selected $Zn_{(1-x)}Mg_xO$ and $Zn_{(1-x)}Mg_xO$:Al layers deposited on Si substrates, an aluminum-doped ZnO (AZO) film of ∼200 nm thickness was grown with the same ALD deposition system using DEZ, DI, and TMA as zinc, oxygen, and aluminum precursors, respectively. The deposition parameters were chosen on the basis of an established ALD deposition routine with, in this case, purging times reduced to 4 s and 280 °C as growth temperature.[24,25] Similarly to what was previously reported in Refs. 24 and 25, the carrier concentration (n), mobility (μ), and ρ of the AZO layers fluctuated in the $(3-6)\times 10^{20}$ cm^{-3}, $(9-11)$ cm^2 V^{-1} s^{-1}, and $(1-2)\times 10^{-3}$ Ω cm ranges, respectively.

B. Contacting and device fabrication

Al/Au Ohmic contacts on the front AZO layer were deposited by sputtering/e-beam evaporation with the Kurt J. Lesker PVD 75 thin film deposition system. These top contacts were circles of ∼1.5 mm^2 area with the Au top layer ∼30 nm thick added only to prevent Al (film thickness ∼100 nm) oxidation. The sample size was ∼5 × 5 mm [see the inset in Fig. 3(a) for a schematic view]. To realize the test solar cells, selected p-Si/$Zn_{1-x}Mg_xO$:Al/AZO structures were cut into ∼1 × 1 cm samples and a ∼200 nm thick Al busbar with a finger contact pattern was sputtered by using the same PVD thin film deposition system. The active to dark/total area ratio of the realized test solar cells was (87 ± 3)% [see the inset in Fig. 11(a) for a front picture]. Finally, Al/Au bilayers (∼100/∼30 nm) on the corner of the ZnO-based films grown on glass and quartz substrates were also sputtered/evaporated using the same PVD setup to serve as Ohmic contacts for Hall measurements.

C. Layers characterization

Energy-dispersive x-ray spectroscopy (EDS) performed with a scanning electron microscope (SEM) Hitachi SU-70 at 5 or 6 kV accelerating voltage was used to determine the Mg and Al atomic contents in the single layers. First, these measurements were used to verify that, as expected and shown in Fig. S1, the Mg content with respect to the sum of the Zn, Mg, and Al atomic contents increased linearly with a proportionality constant equal to 1 with respect to the ratio between the Mg number of ALD cycles and the sum of the Zn, Mg, and Al number of ALD cycles. Furthermore, the same measurements were also used to calculate the Mg content (x), that is, the ratio between the Mg content and the sum of the Zn and Mg ones. SEM front and cross-sectional images after cleaving the layers were also acquired with the same setup operated in the secondary electrons mode (SE). Cross-sectional images were used to measure the film thickness that was confirmed by using a NanoCalc 2000s thin film reflectometer. The structural properties of the ZnO based layers were studied using a PANalytical X'Pert Pro Alpha1 MPD x-ray diffractometer (XRD) with locked-coupled $\Theta - 2\Theta$ scans using the Cu $K\alpha_1$ ($\lambda \sim 1.5406$ Å) monochromatic radiation. In order to extract the signal from the whole volume of the sample under study, the diffraction patterns were collected in the Bragg–Brentano geometry using a semiconductor strip detector in the scanning mode with a 2.122° 2Θ active range. The samples were spinning at an angular velocity of 12.6 rad s^{-1} during the measurements. The room temperature (RT) electrical parameters of the layers were extracted from Hall effect measurements performed in the dark using a RH2035 PhysTech system equipped with a permanent magnet producing a magnetic field of ~0.4 T. The measurements were executed in the van der Pauw configuration on the ZnO based films deposited on glass and quartz substrates. The experimental results were corrected for the contact size contribution as described in Ref. 26. Standard cross-sectional transmission electron microscopy (TEM) samples were prepared by grinding and ion-polishing with a PIPS ion polishing system from Gatan. The samples' local structure and composition were investigated by high-resolution scanning transmission electron microscopy (STEM) using a monochromated FEI Titan G2 60-300 microscope operated at 200 kV and equipped with a Super-X EDS Bruker detector. Finally, the secondary mass spectrometry measurements shown in the supplementary material were conducted with a Cameca IMS 6f microanalyzer using a primary beam of 5.5 keV Cs ions. A constant erosion rate was assumed for depth calibration in this case.

D. Device characterization

The resulting devices were characterized by current density vs voltage (J–V) and capacitance vs voltage (C–V) measurements carried out at RT using a Keithley 2601A and an Agilent E4980A current and LCR meter, respectively. During the measurements, the temperature was monitored with a thermocouple and a HH11C thermocouple reader. In the latter case, *ac*-probing frequencies and an *ac*-probing voltage in the 1 kHz–1 MHz range and equal to 30 mV (root mean square value) were used, respectively. Successively, current vs voltage (I–V) under illumination, η and external quantum efficiency (EQE) measurements were performed on the same devices and the test solar cells using a Bentham PVE300 photovoltaic QE system. The measurements were done under STC, i.e., under the standard terrestrial spectra of AM1.5G and temperature equal to 25 °C. The solar cells/test device parameters presented were calculated using the effective active area of the devices and extracted with the IV Curve Fitter v.1.8 ©software using the standard two-diode model.[27]

III. RESULTS AND DISCUSSION

A. Electrical characteristics of the as-grown layers and devices

The electrical properties of the $Zn_{(1-x)}Mg_xO$ and $Zn_{(1-x)}Mg_xO$:Al films deposited on soda-lime glass vs x are reported in Fig. 1(a) with the corresponding Al atomic content being shown in Fig. 1(b). By introducing Al, an order of magnitude increase in n up to ~4 $\times 10^{20}$ cm^{-3} was achieved. To this increase corresponds a factor 2 decrease of μ. Considering the low Mg alloying level in these layers, the observed drop is consistent with the increased ionized impurity scattering related to the Al donor activity. Furthermore, as discussed hereafter, charged compensating centers, neutral complexes are most probably present as well, thus providing additional scattering centers that contribute to further reduce μ. No significant changes in the film's electrical

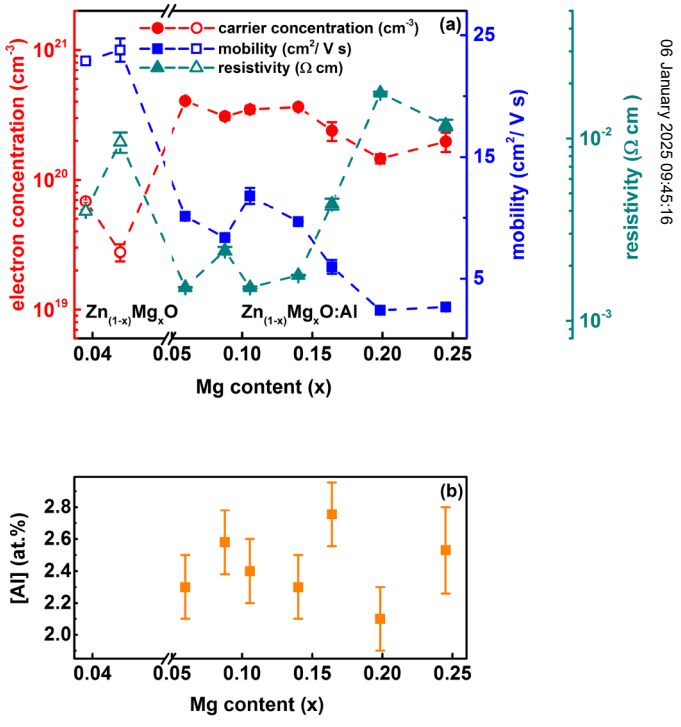

FIG. 1. (a) n, μ, and ρ vs Mg content of the $Zn_{(1-x)}Mg_xO$ and $Zn_{(1-x)}Mg_xO$:Al layers on soda-lime glass. Unfilled symbols indicate depositions where no Al was introduced. (b) Fluctuation of the Al at. % content vs the Mg one in the same samples.

characteristics were found for samples in the $Zn_{0.94}Mg_{0.06}O$:Al–$Zn_{0.86}Mg_{0.14}O$:Al range, while a conductivity drop was observed to occur starting from the $Zn_{0.84}Mg_{0.16}O$:Al sample related to both a reduced μ and n, with the latter indicating a less effective doping activity of Al for higher Mg contents. For the $Zn_{(1-x)}Mg_xO$:Al layers with x varying in the ~0.20–0.24 range, n, μ, and ρ resulted equal to ~1.7 $\times 10^{20}$ cm^{-3}, ~2.2 cm^2 V^{-1} s^{-1}, and ~1.9 $\times 10^{-2}$ Ω cm, respectively. These values are similar to what was previously reported for films grown by ALD and CVD,[28,29] while a further annealing in In presence was found to be necessary to achieve comparable results in the case of sputtered $Zn_{(1-x)}Mg_xO$:Al layers.[30] The decrease in n, μ, and conductivity with increasing Mg content seen to occur from the $Zn_{0.84}Mg_{0.16}O$:Al sample was already reported and attributed mainly to the increase in the reduced electron effective mass caused by Mg alloying.[30] However, as a look at Eq. (6) reveals, the effective mass increase is limited to a factor of ~1.2, which is not enough for explaining the observed factor ~3 decrease of μ. In this respect, it should be noted that the Al content in the samples analyzed varied in the range of ~2.1–2.8 at. %, as shown in Fig. 1(b). This corresponds to an average Al concentration of ~ 2×10^{21} cm^{-3}. Comparison with the n values measured [see Fig. 1(a)] reveals that the Al doping efficiency is ~10%–20%, similarly to what was previously reported in the case of ZnO:Al (see, for example, Ref. 31 and references therein).[32] Such a low activation ratio is partly specific to ALD grown films and has been attributed to the layered/non uniform Al distribution causing dopant clustering, Al incorporation in secondary insulating species, and/or Al segregation at the grain boundaries and interfaces.[33,34] Indeed, the STEM analysis revealed that the films present a columnar structure with the expected nanolaminate Mg and Al distribution within each column as shown in Figs. 2(a), 2(c), and 2(d) (see also Fig. S2 in the supplementary material). Here, it is worth pointing out that, however, the Al atoms' distribution in the films is far from the idealized case, i.e., placed only one lattice plane. In fact, it has a full width half maximum (FWHM) of ~2 nm in the depth direction with a peak to peak distance of ~4 nm, as evidenced by the Al intensity profile extracted from the EDS signal displayed in Fig. 2(e) (for the Mg case, refer to Fig. S2 and the corresponding caption in the supplementary material). This widening of the Al distribution profile has been attributed to the TMA etching effect when reacting with the ZnO-based surface.[33] Furthermore, the DEZ and MCp2Mg steric hindrance could also significantly contribute to limit the layered growth, thus promoting the more random incorporation of Al.[35] In addition, in the present work, the depositions were performed outside the ALD window and for that matter, desorption of the main precursors also occurs.[36] Overall, the Al distribution FWHM was found to be independent from the Mg introduced as a comparison between Figs. 2(e) and S2(c) and S2(f) in the supplementary material reveals. Moreover, considering that the Al doping efficiency in the case of magnetron sputtered ZnO is ~30%–50%, it suggests that the localization related effects roughly account for a ~20%–30% deactivation by assuming a similar weight of the remaining mechanisms.[37] This, even though, in our case, STEM and XRD measurements did not provide any evidence of precipitates, additional phases or Al segregation, that are, therefore, if present, below the detection limit (see Figs. 7 and S2–S5 in the supplementary material). Another physical mechanism that is anticipated to limit the Al doping efficacy is related to the formation of Al-V_{Zn} complexes.[38,39] Concerning the latter, self-compensation effects involving V_{Zn} were shown to explain similar low Ga doping efficiencies in $Zn_{(1-x)}Mg_xO$ layers.[40] Hence, even though a more detailed study would be required to address firmly the exact interplay between the physical mechanisms above mentioned, this is, most probably, a

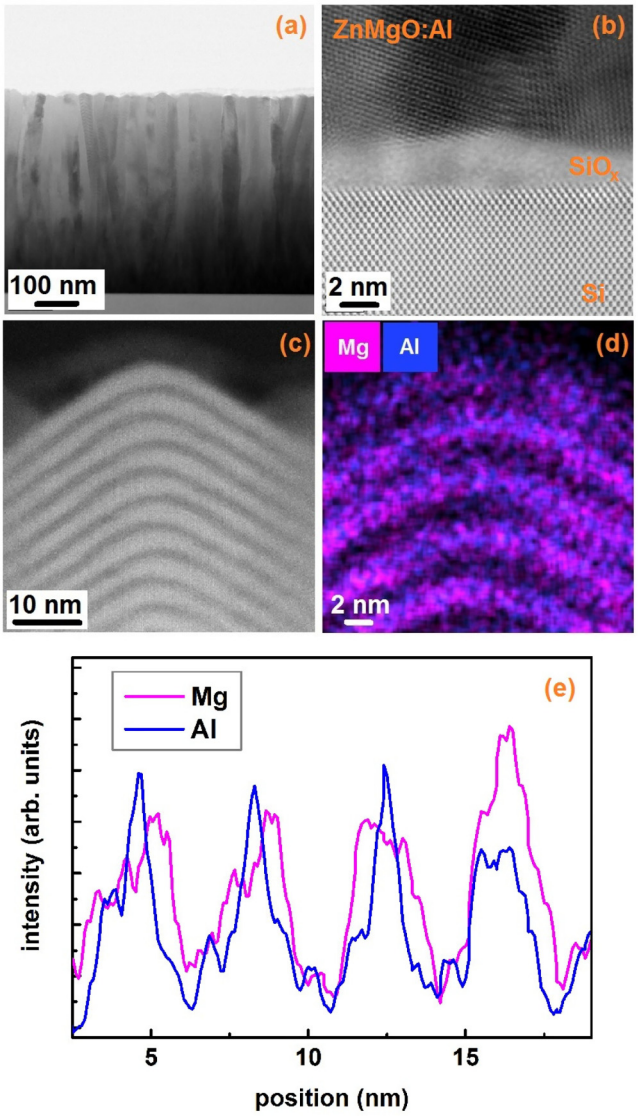

FIG. 2. (a) Cross-sectional annular bright field (ABF) STEM image of the whole $Zn_{0.94}Mg_{0.06}O$:Al layer. (b) ABF STEM view of the $Zn_{0.94}Mg_{0.06}O$:Al/Si interface taken in the [110] substrate orientation. The thickness of the SiO_x interfacial layer was found to vary in the ~2–3 nm range in the investigated samples. (c) High-angle annular dark field (HAADF) STEM image of one column tip. (d) EDS elemental mapping image of the topmost part of the column tip shown and in (e) the central part Mg and Al intensity profiles of the EDS signal.

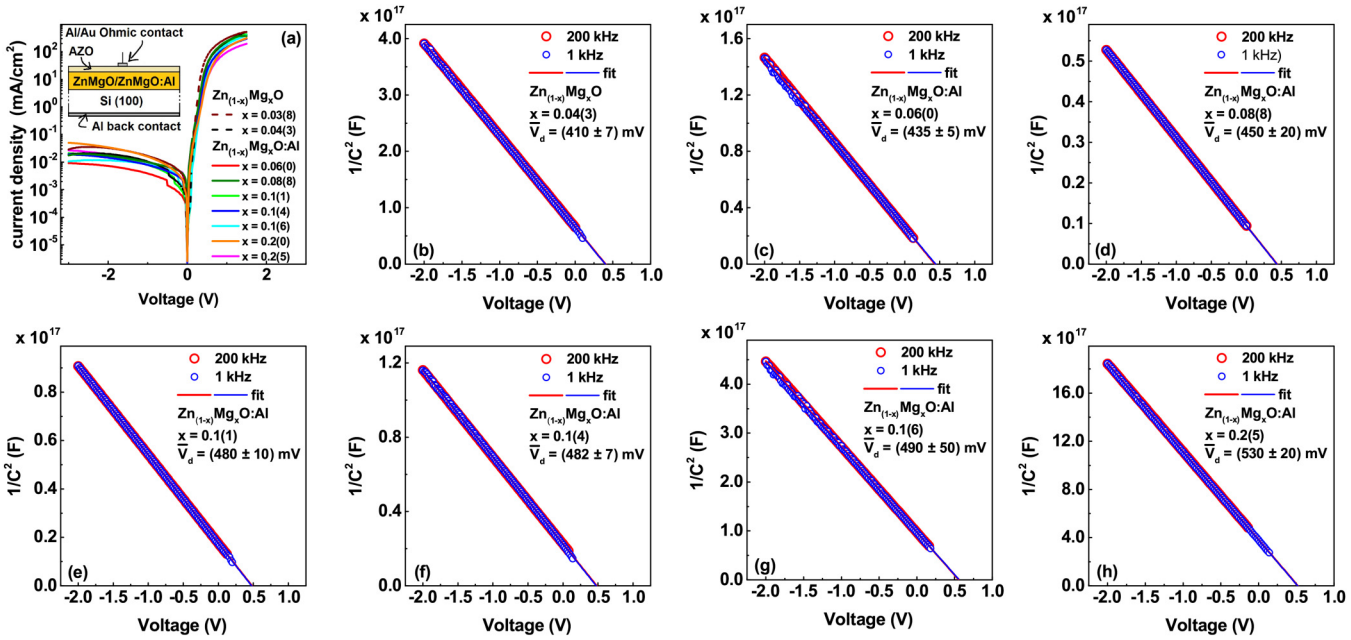

FIG. 3. (a) J–V characteristics vs Mg content collected at RT in the dark with a schematic cross-sectional view of the test devices shown in the inset. (b–h) Plot of $1/C^2$ vs applied voltage measured at 200 and 1 kHz for selected structures with different Mg content; the linear fits used to estimate $\overline{V_d}$ and the corresponding values extracted from averaging among different samples belonging to the same batch and the five different probing frequencies used are reported as well.

factor contributing significantly to the reduced Al donor activity also in the samples analyzed here. Then, the n decrease for Mg contents $x > 0.14$ suggests a reduction in the formation energy of the compensating/neutral center/s involved in lowering the Al doping efficiency with these defects also contributing to lower μ in the same layers.

To test the applicability of such layers to the case of n-ZnO/p-Si based solar cells, the device design already adopted in Ref. 20 and displayed in the inset of Fig. 3(a) was used. The J–V dark characteristics of selected test devices are shown in Fig. 3(a) for all the Mg content investigated. It can be seen that the analyzed samples showed similar J–V dark characteristics independent of the Mg content exhibiting four to five orders of magnitude rectification ratio in the $[-1, +1]$ V voltage range. Note that, as evident from Fig. 2(b), the realized samples are actually n-$Zn_{(1-x)}Mg_xO$/SiO_x/p-Si and n-$Zn_{(1-x)}Mg_xO$:Al/SiO_x/p-Si heterostructures; however, for simplicity, hereafter, SiO_x will be omitted from the heterojunctions' definition unless it is needed for clarity. The n-$Zn_{(1-x)}Mg_xO$/p-Si and n-$Zn_{(1-x)}Mg_xO$:Al/p-Si heterostructures were further electrically analyzed in order to extract ΔE_C.[20,41,42] That is, the J–V characteristics collected in dark conditions were assumed to follow a standard Shockley diode equation (single exponential model) that includes both series (R_s) and shunt (R_p) resistance,[43]

$$JA = I_S\left(\exp\left(\frac{e(V - R_S JA)}{\nu k_B T}\right) - 1\right) + \frac{(V - R_S JA)}{R_P}, \qquad (1)$$

where A, I_S, e, ν, k_B, and T are the junction total area, the saturation current, the electron charge, the ideality factor, the Boltzmann constant, and the absolute temperature, respectively. Then, R_S and ν were determined following a procedure outlined in Ref. 43. This analysis (not shown) did not evidence any significant changes in ν and R_S vs Mg content with the exception of an increase in R_S for a Mg content equal to ~0.25. Similarly, ν was found to be $\lesssim 2$ in the same Mg content range. The R_S values so extracted were used to establish the proper voltage and frequency interval where the R_S contribution to the measured capacitance can be assumed to be negligible with the upper bound for the testing frequency being $\leq$200 kHz.[44] Here, it should be noted that, as shown above, the $Zn_{(1-x)}Mg_xO/Zn_{(1-x)}Mg_xO$:Al layers are degenerate with $n > 10^{19}$ cm^{-3}, while an effective acceptor concentration (N_a) equal to ~2×10^{15} cm^{-3} is anticipated in the p-Si substrates according to the vendor specifications. That is, the n-$Zn_{(1-x)}Mg_xO$/SiO_x/p-Si and n-$Zn_{(1-x)}Mg_xO$:Al/SiO_x/p-Si heterostructures can be actually modeled as Schottky contacts to p-Si with a SiO_x interlayer. The SiO_x presence introduces a capacitance (C_{ox}) that is in series with the p-Si depleted region one. This contribution, modeling it as a parallel capacitor with a distance between the plates equal to 2–3 nm, as evidenced by the TEM analysis of the interfacial region [see Fig. 2(b)], is $\gtrsim$50 times larger than the highest measured capacitance and, therefore, can be neglected since introducing an ~2% correction. Second, the SiO_x layer thickness allows direct tunneling.[45] In such case, the occupation of defects at the SiO_x/Si interface is expected to be determined by ϵ_F, the RT bulk Fermi level positions with respect to the conduction band in the

$Zn_{(1-x)}Mg_xO$ or $Zn_{(1-x)}Mg_xO$:Al layers. Thus, the corresponding capacitance is in parallel to C_{ox}.[46] Hence, the above-mentioned correction is an upper bound in case of a significative contribution of the defects at the SiO_x/Si interface. Bearing this in mind, the measured C–Vs are essentially equal to the dependence on V of the p-Si depleted region capacitance, i.e.,[41,46]

$$\frac{C}{A} = \sqrt{\frac{\frac{1}{2} q \epsilon_0 \epsilon_{Si} N_a}{(\overline{V_d} - V)}}, \tag{2}$$

where ϵ_0 is the vacuum permittivity, indicating with ϵ_{Si} the relative dielectric constant of Si and with $\overline{V_d}$ the diffusion potential arising at the heterojunction corrected for the contribution of the hole tail at the edge of the depletion region in the p-Si, i.e., $\overline{V_d} = V_d - k_B T/e$. Then, by performing a linear fit of $1/C^2$ vs V for each of the probed frequencies, $\overline{V_d}$ was determined. Examples of this analysis are shown in Figs. 3(b)–3(h). Here, it is worth stressing that using C–V measurements and Eq. (2) for extracting V_d is a robust method in the case of the examined samples even in case defects at the SiO_x/Si interface are present. If such defects are assumed uniformly distributed in the examined voltage range, their contribution to the extracted V_d can be evaluated using the extension of Eq. (2) first proposed in Ref. 47. In detail, even taking into account possible non stochiometry effects, a $\lesssim$10 mV correction to V_d corresponds to the reported defect density at the intrinsic Fermi level position equal to $\sim 5 \times 10^{12}\,cm^{-2}\,eV^{-1}$ in the case of native SiO_x.[48] That is, this contribution is equal to the typical error on the measurements [see Figs. 3(b)–3(h)] and can be, therefore, neglected.

Subsequently, ΔE_C was determined (see also the inset of Fig. 4) according to

$$\Delta E_C = E_{Si} - eV_d - \delta_{Si} + \epsilon_F, \tag{3}$$

where E_{Si} is the RT Si bandgap, while δ_{Si} is the RT bulk Fermi level position with respect to the valence band in Si. In employing Eq. (3), ϵ_F was taken as positive since, according to the Hall measurements above discussed, all the examined $Zn_{(1-x)}Mg_xO$/$Zn_{(1-x)}Mg_xO$:Al layers were degenerate.

To evaluate δ_{Si} and ϵ_F, the hole concentration in the p-Si wafer (p_{Si}) and the electron concentration in the n-$Zn_{(1-x)}Mg_xO$/n-$Zn_{(1-x)}Mg_xO$:Al layer are necessary. The N_a values, as extracted from C–V profiling measurements, were used for the former; on the other hand, the latter was assumed to be equal to n, i.e., the electron concentrations of the $Zn_{(1-x)}Mg_xO$ and $Zn_{(1-x)}Mg_xO$:Al layers deposited on soda-lime glass and shown in Fig. 1(a). Then, using the measured p_{Si} and n, if the density of states reduced effective masses in the valence and conduction band for Si (m_v^*) and $Zn_{(1-x)}Mg_xO$/$Zn_{(1-x)}Mg_xO$:Al ($m_{c,x}^*$) are known, δ_{Si} and ϵ_F can be easily evaluated by inverting the carrier concentration vs Fermi level formulae for a nondegenerate,

$$p_{Si} = N_a = 2\left(\frac{m_v^* m_e k_B T}{2\pi\hbar^2}\right)^{\frac{3}{2}} e^{\frac{-\delta_{Si}}{k_B T}}, \tag{4}$$

and a degenerate semiconductor,

$$n = N_d = \frac{1}{\pi^2\hbar^3}\int_0^\infty \frac{(m_{c,x}^* m_e)^{\frac{3}{2}}\sqrt{2E}}{1+\exp\left(\frac{E-\epsilon_F}{k_B T}\right)}\,dE, \tag{5}$$

where m_e, $\hbar$, and E are used to indicate the electron rest mass, the reduced Planck constant, and the electron energy referred to the conduction band edge, respectively. On the other hand, N_d refers to the effective donor density in the $Zn_{(1-x)}Mg_xO$/$Zn_{(1-x)}Mg_xO$:Al layers. In the present analysis, m_v^* was set to 1.15 (see Ref. 49). On the contrary, the reported experimentally determined effective masses for $Zn_{(1-x)}Mg_xO$ are in reality reduced effective masses.[29,30] Furthermore, ZnO presents a non-parabolic conduction band shape and indications of non-parabolicity have been found also in the case of first-principles calculation for $Zn_{(1-x)}Mg_xO$.[50] Hence, not only the Mg dependence of $m_{c,x}^*$ but also non-parabolicity effects should be taken into account for a proper evaluation of ϵ_F. Theoretical calculations indicate that $m_{c,x}^*$ increases with Mg concentration with a proportionality factor ranging from 0.22 x to 0.27 x.[40,51] Therefore, on the basis of what is written above and considering the two effects as independent, the following approximate dependence for $m_{c,x}^*$ on E and x was used:[52]

$$m_{c,x}^* = (m_{c,0}^* + 0.25x)(1+2\alpha E) = m^*(x)(1+2\alpha E), \tag{6}$$

where the intermediate value of 0.25 was chosen for the Mg contribution, while α and $m_{c,0}^*$ were set to $0.33\,eV^{-1}$ and 0.28 according to Ref. 53 and on the basis of previous work on Hall data simulations (see Ref. 54 and references therein), respectively. Note that by using Eq. 6, it was implicitly assumed that Al doping in the at. % range has no effect on the conduction band structure as theoretically predicted.[55]

Here, it is worth noticing that in the approach used for extracting ΔE_C, N_a and N_d are considered uniform as evident from Eqs. (2) and (3) as well as differences between n in the $Zn_{(1-x)}Mg_xO$/$Zn_{(1-x)}Mg_xO$:Al films deposited on the soda-lime glass, which are the samples actually measured, and the emitter layers on the realized structures are neglected. Differences in n between the $Zn_{(1-x)}Mg_xO$/$Zn_{(1-x)}Mg_xO$:Al emitter layer and the films deposited on the soda-lime glass cannot be excluded, but they are anticipated to be comparable to the variation observed in the case of layers deposited on quartz and soda-lime glass during the same deposition process, which were found to be $\lesssim$20% and thus similar to the measurement errors and therefore not relevant. On the other hand, non-uniformities in the interfacial region cannot be excluded. In detail, if the equivalent of Eq. (2) for heterostructures is used, depth intervals equal to $\sim$0.4–1.5 μm and < 0.4 nm in the p-Si and n-$Zn_{(1-x)}Mg_xO$/n-$Zn_{(1-x)}Mg_xO$:Al side of the heterostructure relate to the voltage range used.[41] Non-uniformities in the effective acceptor and donor concentrations on the p-Si and n-$Zn_{(1-x)}Mg_xO$/$Zn_{(1-x)}Mg_xO$:Al sides of the heterojunction outside or with length scales larger than the probed depths by C–V measurements would result in an apparent ΔE_C since ϵ_F, as extracted from Hall measurements, would not correspond to the actual ϵ_F in the interfacial region with a similar argumentation

holding for the Si part of the heterojunction. However, while such effect can be reasonably excluded to occur on the Si side, this might be the case for the $Zn_{(1-x)}Mg_xO/n - Zn_{(1-x)}Mg_xO$:Al layers considering the limited depth investigated as well as the expected presence of defects in these layers close to the SiO_x interface. This represents a potential source of error in the determination of ΔE_C according to the procedure used here; this issue is discussed more in detail at the end of the following Subsection.

The results of the analysis outlined above are presented in Fig. 4. The most striking feature is the ∼0.48 eV increase in ΔE_C, that is rising from ∼0.5 eV up to ∼1 eV following the Al introduction into the $Zn_{(1-x)}Mg_xO$ layers, while increasing the Mg content from 0.04 to 0.06. As above mentioned, all the $Zn_{(1-x)}Mg_xO/Zn_{(1-x)}Mg_xO$:Al layers are degenerate. Then, bandgap narrowing with the corresponding conduction band lowering is indeed expected in the samples. That is, the experimentally extracted ΔE_C is carrier concentration dependent. Hence, to derive more general conclusions, ΔE_C should be corrected for this contribution as described in the following Subsection.

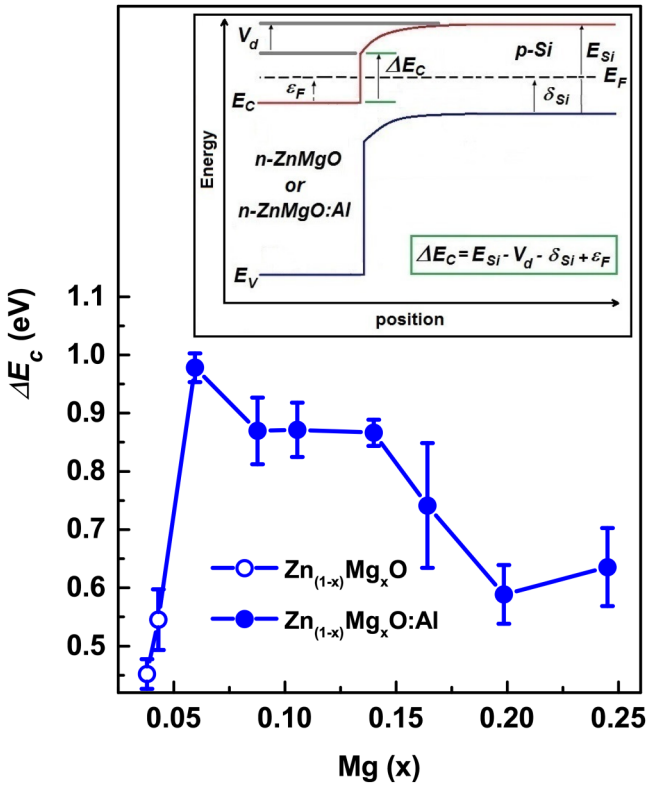

FIG. 4. The conduction band misalignment, ΔE_C, vs Mg content as extracted from C–V and Hall measurements. The unfilled circles refer to samples without Al. In the inset is a schematic view of the equilibrium band diagram corresponding to the structures electrically characterized with the conduction and valence band edge labeled as E_C and E_V, respectively. All the devices investigated presented a $\Delta E_C > 0$, thus corresponding to the shown type II band alignment. Furthermore, in all samples, the $Zn_{(1-x)}Mg_xO$ and $Zn_{(1-x)}Mg_xO$:Al layers were degenerate. For that matter, ϵ_F is depicted above E_C on the film side and the Schottky contact approximation is used in drawing the bands' alignment sketch. The extension of the band-bending region is not drawn to scale. For the interfacial region, see Fig. 6.

B. Impact of the Al, Mg content, and the SiO_x interlayer on the conduction band misalignment

Two main physical mechanisms contribute to the resulting conduction band lowering: Many body effects, i.e., repulsion between electrons as a consequence of the Pauli exclusion principle and Coulomb repulsion as well as the interaction of the electrons with the donors. Hereafter, the former and latter contributions are indicated as ΔE_C^{ee} and ΔE_C^{ei}, respectively. Several methodologies have been proposed to take these effects into account.[56–59] Among them, the plasmon pole approximation for the dielectric response in the self-energy formalism introduced by Inkson[56] has been proven to be essentially equivalent to more complex approaches in the case of Si,[59] and it has been further generalized to III–V semiconductors.[60,61] This formalism is used here. However, it is worth pointing out that, despite being widely used, the non-parabolicity corrections to ΔE_C^{ee} and ΔE_C^{ei} have been overlooked in the literature as discussed in more detail hereafter. Hence, the calculations presented in Refs. 56 and 57 were reiterated taking into account the non-parabolic structure of the conduction band. Then, it can be seen that the results of the conduction band shift related to the many body effects equal[62]

$$\Delta E_C^{ee} = -\frac{e^2 \bar{k}_F}{2\pi^2 \epsilon_0 \epsilon_r} - \frac{e^3}{8\pi}\sqrt{\frac{3n}{2\epsilon_F(\epsilon_0\epsilon_r)^3}} \times \left(1 - \frac{4}{\pi}\tan^{-1}\left(\frac{\bar{k}_F}{\lambda_{TF}}\right)\right), \tag{7}$$

where

$$\bar{k}_F = \frac{1}{\hbar}\sqrt{2m^*(x)(\epsilon_F + \alpha\epsilon_F^2)}$$

and

$$\lambda_{TF} = \sqrt{\frac{3e^2 n}{2\epsilon_F \epsilon_0 \epsilon_r}},$$

where λ_{TF} is the Thomas–Fermi wave vector. On the other hand, $\bar{k}_F$ reduces to the ordinary Fermi wave vector expression in the case of a parabolic conduction band. That is, since the frequency integrated plasmon pole expression for the dielectric constant, when only the quadratic term of the wave vector dependence is included, does not depend on the effective mass, the non-parabolicity affects only the Green's function integral upper limit, that is $\bar{k}_F$.

Differently, the contribution related to the interaction of the electrons with the donors can be calculated using the time independent second-order perturbation theory.[57] Hence, the integrand involves a sum weighted by the energy difference between the possible electron levels and, therefore, in this case, the conduction band non-parabolicity affects the integrand directly. By performing the calculations, the following closed form was found for this

contribution:

$$\Delta E_C^{ei} = -\frac{e^4 N_D m^*(x)}{\pi^2\hbar^2(\epsilon_0\epsilon_r)^2} \times \left(\frac{\hbar}{\overline{\lambda}_{TF}^2}\sqrt{\frac{\alpha}{2m^*(x)}} + \frac{\tan^{-1}\left(\frac{C}{\overline{\lambda}_{TF}\hbar\sqrt{\frac{2\alpha}{m^*(x)}}}\right)}{2\overline{\lambda}_{TF}^3 C} \right), \tag{8}$$

with

$$C = \left(1 - \overline{\lambda}_{TF}^2 \frac{2\alpha\hbar^2}{m^*(x)}\right)^{\frac{1}{2}}$$

and

$$\overline{\lambda}_{TF}^2 = \frac{e^2}{\epsilon_0\epsilon_r}\frac{\sqrt{2m^*(x)^3}}{\pi^2\hbar^3}\sqrt{\epsilon_F + \alpha\epsilon_F^2}(1 + 2\alpha\epsilon_F),$$

where the latter is the Thomas–Fermi wave vector corrected for the non-parabolicity of the conduction band, an expression that reduces to λ_{TF} in the parabolic case. On the other hand, N_D is the total concentration of ionized donors acting as scattering centers. Here, it is worth pointing out that Eqs. (7) (with the exception of the first term) and (8) differ considerably from the equivalent ones used in previous reports (cf. Refs. 63 and 64).

As discussed in Sec. III A, only 10%–20% of the Al is actually acting as a donor with the remaining not providing free carriers because, most probably, it is involved in the formation of charged deep defects and/or neutral complexes at least partially. Considering that such defects are expected to present smaller capture cross sections with respect to shallow centers, then, their interaction with the conduction band electrons can be neglected, at least in the first approximation. Hence, in the calculations hereafter presented, N_D was considered equal to n.

Then, if the contributions of the electron–electron and electron–donor interactions are known, ΔE_C^0 (ΔE_C in the low doping regime) can be evaluated as

$$\Delta E_C^0 = \Delta E_C - \Delta E_C^{ee} - \Delta E_C^{ei}. \tag{9}$$

The values so obtained are displayed in Fig. 5, while the correction related to the conduction band lowering is shown in the inset.

It can be seen that the extracted ΔE_C^0 after the abrupt increase of ~0.24 eV, as a consequence of Al introduction, was found to approximately linearly decrease with Mg content from (0.59 ± 0.02) down to (0.31 ± 0.07) eV. From a least squares regression fit of the $Zn_{(1-x)}Mg_xO$:Al related data, a linear decreasing factor of ΔE_C^0 vs Mg content and an intercept equal to (−1.7 ± 0.2) eV and (0.69 ± 0.03) eV were found, respectively.

To get more insight into the observed conduction band alignment and evaluate the contribution of each component of the heterostructure, the interface-induced gap states (IFIGS) model can be used. This approach has been successfully applied to describe a wide variety of heterostructures based on elementary and compound semiconductors with a reported accuracy of ~0.15 eV.[41,65,66]

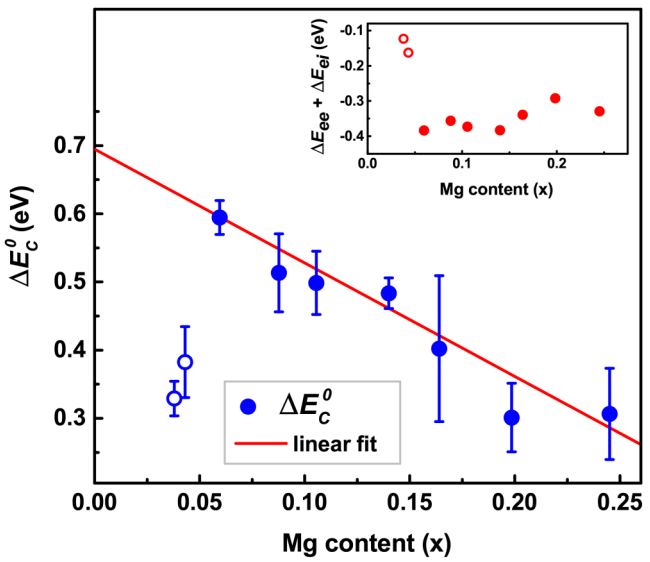

FIG. 5. The dependence of ΔE_C^0 on the Mg content. The total correction to ΔE_C vs Mg content is shown in the inset. Empty and full symbols correspond to ΔE_C^0 extracted from the analysis of $Zn_{(1-x)}Mg_xO$ and $Zn_{(1-x)}Mg_xO$:Al heterostructures, respectively. The red line is a least squares regression fit of the $Zn_{(1-x)}Mg_xO$:Al data only.

Furthermore, it has been recently proposed for understanding metal-ultrathin insulator-semiconductor structures and can be, therefore, similarly applied to the samples analyzed here, with the ultrathin insulator being the SiO_x interfacial layer.[67] It is based on the observation that a semiconductor surface (with insulators described as wide-gap semiconductors), due to the periodicity truncation, has a metallic character since the complex wavevectors should also be considered and the corresponding states populate the material bandgap. The level at which these wavefunctions change their character from more valence-like (neutral if occupied) to more conduction-like (neutral if unoccupied) is the so-called branch-point (Φ_{bp}) with its energy position referring to the valence band maximum throughout this work. Considering its definition, Φ_{bp} is expected to be the semiconductor equivalent of the Fermi level in a metal when it comes to the band alignment.[68] Therefore, on the basis of what written above, the Φ_{bp}s of all the materials in the heterostructure should be aligned. Thus, the interfacial valence-band offset between the two semiconductors (ΔW_v) is related to the energy distances of the branch-points from the valence band maxima, hereafter indicated as Φ_{bp}^{ZnMgO} and Φ_{bp}^{Si} for $Zn_{(1-x)}Mg_xO$ and Si, respectively. Furthermore, considering that the materials put in contact present substantially different electronegativities, a correction term that takes into account the intrinsic dipoles forming at the interfaces should be included as well, with its effect on the otherwise aligned Φ_{bp}s shown in Fig. 6. Then, ΔW_v can be determined using the equation[65,67]

$$\Delta W_v = \Phi_{bp}^{ZnMgO} - \Phi_{bp}^{Si} + S(X_{ZnMgO} - X_{Si}), \tag{10}$$

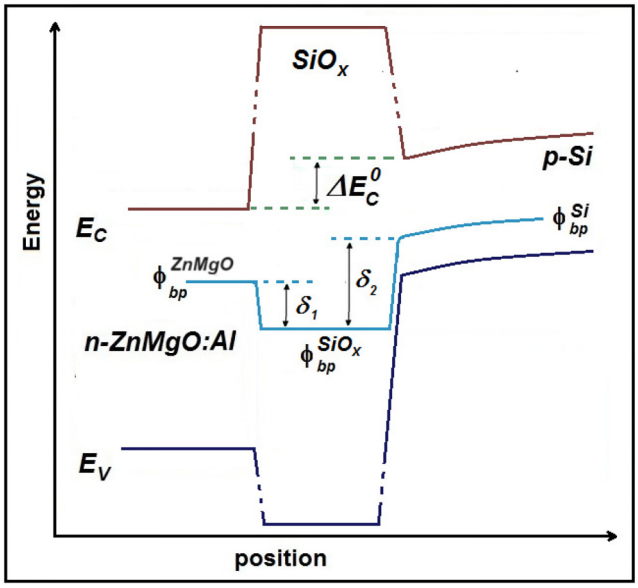

FIG. 6. A schematic view of the interfacial band diagram corresponding to the structures electrically characterized with focus on the correction to the band alignment related to the intrinsic dipole forming at the $Zn_{(1-x)}Mg_xO$:Al/SiO_x and SiO_x/Si interfaces. $S(X_{ZnMgO} - X_{Si})$ in Eq. (10) is equal to $\delta_2 - \delta_1$, that is the difference between the two interfacial intrinsic dipole contributions. The extension of the band-bending region is not drawn to scale.

where X_{ZnMgO} and X_{Si} are used to indicate the Miedema's electronegativities of $Zn_{(1-x)}Mg_xO$ and Si, respectively, while S follows the empirical dependence on the SiO_x high frequency permittivity (ϵ_∞),

$$S = \frac{0.86}{1 + 0.1(\epsilon_\infty - 1)^2}.$$

In the present analysis, S was set to (0.6 ± 0.1) eV/Miedema-units. This value is obtained by assuming an isotropic ϵ_∞ in the range of 2.25–4 with the extreme of the interval chosen on the basis of the reported values for SiO_2 and SiO, thus considering possible non-stoichiometric effects.[69] On the other hand, 4.70 and 5.54 Miedema-units were used as values for X_{Si} and X_{ZnMgO}, respectively. The former corresponds to the estimate determined directly by Miedema, while the latter is the geometric mean of the respective values for Zn and O atoms.[65,70] That is, no effect due to Al and Mg alloying has been taken into account, a choice that is justified by the similar Al and Zn Miedema's electronegativities (4.20 instead of 4.10 Miedema-units) as well as the ZnO and MgO close values (5.54 instead of 5.09 Miedema-units). This results in $S(X_{ZnMgO} - X_{Si}) = (0.5 \pm 0.1)$ eV. Then, Eq. (10) yields a Φ_{bp}^{ZnO} of (2.7 ± 0.2) eV using the intercept value extracted from the linear fit of the ΔE_C^0s corresponding to the Al-doped layers, taking $\Phi_{bp}^{Si} = (0.30 \pm 0.09)$ eV from Ref. 23 and assuming a RT bandgap energy for ZnO and Si equal to 3.36 and 1.12 eV, respectively. On the other hand, Φ_{bp}^{ZnMgO} has been assumed to vary linearly between the respective values of the corresponding two binary compound semiconductors, ZnO and MgO, that is,

$$\Phi_{bp}^{ZnMgO} = \Phi_{bp}^{ZnO}(1 - x) + \Phi_{bp}^{MgO}x, \quad (11)$$

as it is generally done.[65] This, even though ZnO and MgO are not isostructural and $Zn_{(1-x)}Mg_xO$, presents a rock salt structure for x $\gtrsim$45.[71] However, theoretical calculations indicate a linear dependence of Φ_{bp} corresponding to the wurtzite phase when x is varied from 0 up to 1, with a deviation of $\leq$ 15% if the rock salt structure is considered instead, thus justifying the approach used here.[72] Hence, using Eq. (11), Φ_{bp}^{ZnO} and the proportionality factor extracted from the linear fit of the ΔE_C^0s corresponding to the Al-doped layers, Φ_{bp}^{MgO} is found equal to (3.6 ± 0.4) eV, where, in this case, a dependence of the $Zn_{(1-x)}Mg_xO$ bandgap on the Mg content of 2.51 was assumed.[73]

Here, it is worth noticing that Eq. (10) should be modified in case the $Zn_{(1-x)}Mg_xO$:Al layer is strained and/or formation of an electrical double layer subsequent to the Al introduction, Al segregation at the interface, or polarity effects are present.[65,66] Each of these factors or a combinations of them could potentially explain the observed $\Delta E_C^0 \sim 0.27$ eV difference between the $Zn_{(1-x)}Mg_xO$ value and the expected one according to the $Zn_{(1-x)}Mg_xO$:Al layers' linear fit. To estimate their contributions first, the morphological and structural properties of the $Zn_{(1-x)}Mg_xO$ and $Zn_{(1-x)}Mg_xO$:Al layers were studied further by SEM and XRD with the collected XRD patterns, cross-sectional and front SEM views shown in Figs. 7 and S5(a)–S5(d), respectively [for a full overview of the dependence, the XRD patterns on the Mg atomic content, see Figs. S5(e) and S5(f) in the supplementary material]. Overall, the layers were polycrystalline and exhibited a wurtzite structure. In addition, it can be seen that no secondary phases related to, for example, clusters based on Al and/or Mg compounds, were observed indicating that, if present, their relative amount and/or size is, also in this case, below the detection limit or they are amorphous. In detail, the concomitant appearance of the 11.0 and 10.0 reflections was observed by introducing Al and keeping constant the Mg content with the presence of these peaks being consistent with the observed wedge-shaped crystallite morphology of the surface considering the wurtzite structure (see Figs. S4 and S5 and corresponding captions in the supplementary material for more details). On the other hand, the 10.1 reflection was found to be suppressed by Al introduction. Furthermore, the 00.2 reflection was still clearly detectable for $Zn_{(1-x)}Mg_xO$:Al layers with $\leq$ 0.1(6) Mg content. As shown in Fig. 7(e), increasing the Mg content further has been found to drastically suppress the growth in the *c*-direction, with the dominating peaks being the 10.0 and 11.0 reflections at the highest Mg content investigated in the present work. Thus, polarity corrections can be excluded in the layers with x > 0.16. The evolution of the lattice constants *a* and *c* vs Mg content is shown in Fig. 8. Overall, it was found that, in comparison to the relaxed material, the lattice constants of the not intentionally doped $Zn_{(1-x)}Mg_xO$ layers are $\sim -0.2\%$ and $\sim -0.3\%$ strained in the *a* and *c* directions, respectively.[5,73] On the other hand, differently from what has been previously reported, the Al introduction appears to significantly affect only the lattice spacing in the *a*

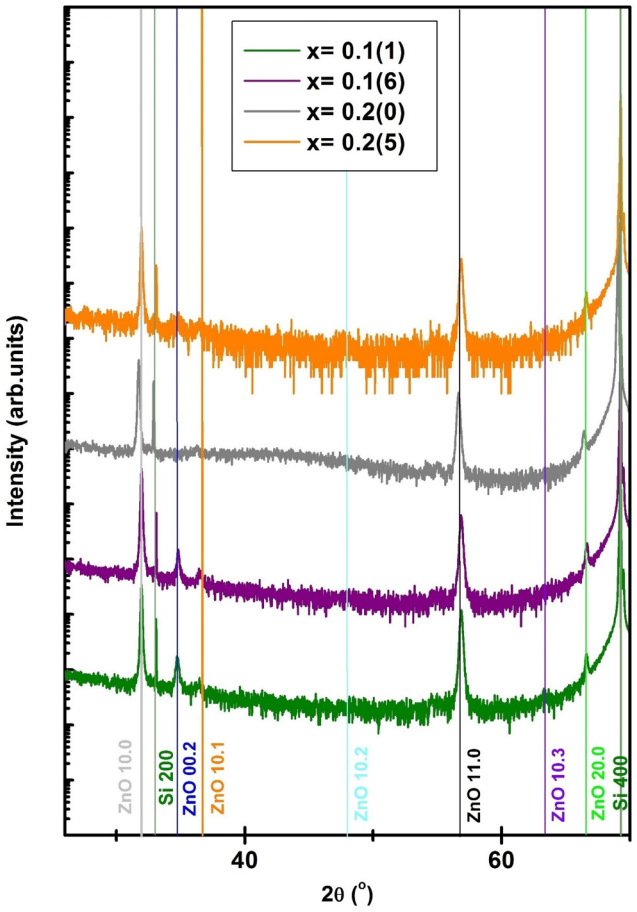

FIG. 7. Comparison between the XRD pattern of the $Zn_{(1-x)}Mg_xO$:Al layers with Mg content equal to 0.1(1), 0.1(6), 0.2(0), and 0.2(5). The peak positions of the bare ZnO are also indicated as reference.

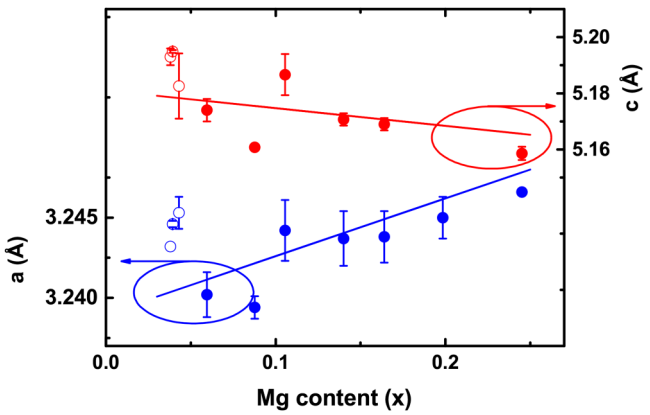

FIG. 8. Dependence of the *a* and *c* lattice constants on the Mg content. Empty circles are the values relative to layers where no Al was introduced. The errors comprehend spatial variations as well as, in the case of the *a* lattice constant, variations between the values extracted using the 10.0 and 11.0 peak positions when both of them were present in the XRD patterns. Solid lines indicate the expected contraction and expansion reported in the case of $Zn_{(1-x)}Mg_xO$ in Refs. 5 and 73 for *c* and *a* lattice constants, respectively.

direction with an additional $\sim -0.1\%$ contraction.[74] Moreover, further addition of Mg is found to shorten the *c*-axis length, while gradually increasing the *a*-axis length with, therefore, a minor impact on the unit cell volume, as expected, considering the similar ionic radius of Zn^{2+} and Mg^{2+}.[73] In Fig. 8, the measured values for the *c*-axis and *a*-axis are compared with the expected contraction and expansion reported in the case of $Zn_{(1-x)}Mg_xO$ in Refs. 5 and 73. It can be seen that agreement was found between the experimental values and the expected trends. That is, it can be concluded that within the experimental errors, the Al introduction does not alter the expected variation of *a* and *c* with Mg incorporation. On the other hand, its impact due to the deformation can be roughly estimated to downshift the conduction band $\lesssim$0.01 eV if the in-plane stress is considered isotropic and 6.05 eV, the conduction band deformation potential evaluated under hydrostatic pressure, is used.[75] That is, assuming that the observed strain is uniform up to the interface, the increase in the *a*-direction strain cannot account for the observed $\sim$0.27 eV ΔE_C^0 increase when Al is introduced. Second, over the full set of samples analyzed, a maximum downshift of $\lesssim$0.05 eV corresponds to the maximum strain observed. Finally, as shown and discussed above and in the supplementary material, despite the morphological and structural changes related to the Al introduction, the 00.2 reflection is still the dominant one both in the $Zn_{0.96}Mg_{0.04}O$ and $Zn_{0.94}Mg_{0.06}O$:Al case with nominally equal Mg content; hence, effects on the bands alignment related to the crystal orientation/polarity are expected to be similar if these two samples are compared. That is, in conclusion, the corrections related to the strain are, in the first approximation, negligible since of the order of the uncertainty on ΔE_C^0 and polarity effects can be excluded as a main cause of its $\sim$0.27 eV increase when Al is introduced.

As mentioned in Sec. II, the first TMA pulse was introduced after a total number of DEZ+DI and MCp2Mg+DI pulses varying in the 13–24 range. This corresponds to a distance from the interface of the first Al-doped layer in the $\sim$2–4 nm range assuming a constant growth rate per cycle (GPC), value that is equal to or slightly larger than the Al distribution FWHM observed by STEM. Therefore, overall, an interplay between Al and the interface cannot be ruled out on the basis of the results presented so far even in the absence of interfacial segregation.[37,76] To exclude such an effect, two additional series of samples with the same nominal Mg content (fluctuating in the x$\sim$0.18–0.20 range according to EDX measurements) and the first TMA pulse introduced after a total number of DEZ+DI and MCp2Mg+DI pulses equal to 96 and 384 were grown (hereafter labeled as II and III, respectively) and electrically characterized. In these films, considering a constant GPC, the first Al-doped layer is expected to be placed $\sim$13 and $\sim$57 nm far from the interface in the former and latter cases, respectively. SIMS measurements performed on this series of samples and shown in Fig. S6 in the supplementary material confirmed the presence of the $Zn_{(1-x)}Mg_xO$ interlayers with its thickness clearly

distinguishable in the case of the III series and equal to ≈ 60 nm, in agreement with the predicted one and [Al] upper limit $\leq 10^{18}$ cm^{-3}. Selected $1/C^2$ curves used to extract V_d are shown in Fig. 9(a) with n of the corresponding $Zn_{(1-x)}Mg_xO$:Al layers deposited on glass displayed in Fig. 9(b). As shown in Fig. 9(b), no dependence of the extracted ΔE_C^0 on the Al position was observed.[77]

In conclusion, no experimental evidence of a possible interplay of Al with the interface was found. In addition, corrections related to strain due to Al and Mg introduction are negligible/within the experimental errors, and polarity effects can be excluded for $x > 0.14$ and, if present, their contribution is similar for $x \sim 0.05$ in layers with and without Al. Overall, these findings rather support the ΔE_C^0 values extracted in the case of the Al-doped layers, while suggesting that the ΔE_Cs for the undoped samples reported in Fig. 4 are apparent values. Indeed, reiterating the analysis based on Eqs. (3) and (9), it is found that the observed ∼0.27 eV difference in ΔE_C^0 between the $Zn_{0.96}Mg_{0.04}O$ and $Zn_{0.94}Mg_{0.06}O$:Al layers can be explained if a ∼0.46 eV downward band bending (E_{bb}) toward the interface with SiO_x is present. On the other hand, ϵ_F is found in the ∼0.57–0.47 eV range in the Al-doped layers with $x \leq 0.14$. That is, ϵ_F is large enough for compensating E_{bb} in these samples and, therefore, the extracted ΔE_C^0s are reliable in this case. Here, it is also worth underlining that, beside variation in the effective N_d, other factors, like the presence of positive charges at the $Zn_{(1-x)}Mg_xO/SiO_x$ interface (externally introduced), in the SiO_x[78] or polarity induced cannot be excluded on the basis of the data presented above and are most probably contributing to E_{bb} considering its relative large value. Furthermore, as shown in Fig. 5 the ΔE_C^0 values are, within the experimental errors, in agreement with the expected trend also for $x > 0.14$ where ϵ_F is in the ∼0.38–0.28 eV range. This suggests a reduced E_{bb} in these samples pointing to an effective N_d reduction in the interfacial region and/or lower polarity contribution consistent, at least qualitatively, with the above presented effects of Mg introduction on the layers' structural and electrical properties. However, further dedicated studies are required to firmly confirm this scenario.

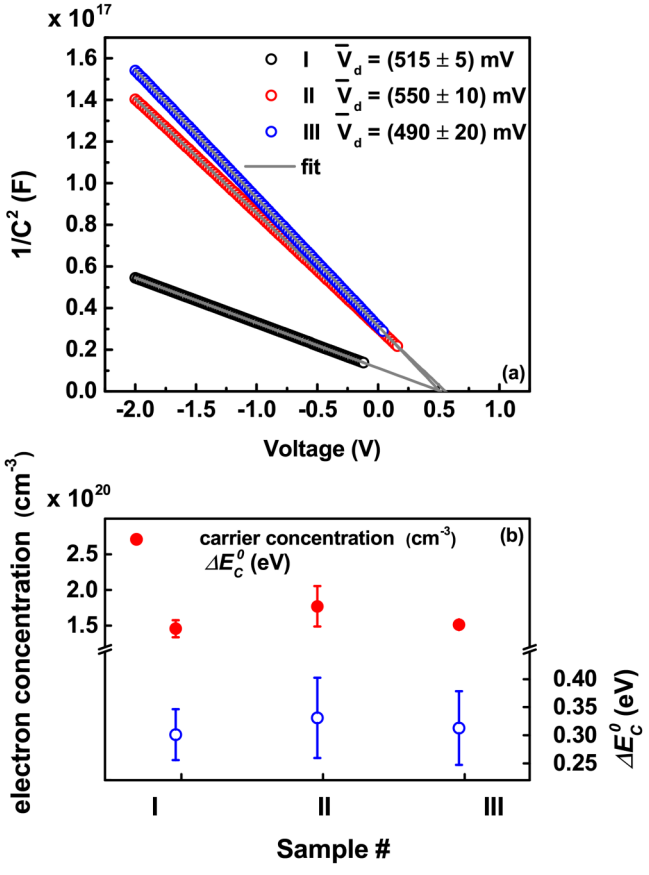

FIG. 9. (a) Plot of $1/C^2$ measured at 200 kHz vs the applied voltage in the case of three selected test structures with the extracted $\overline{V_d}$ (average between the five different probing frequencies used) reported in the figure as well. (b) n and the extracted ΔE_C^0s. In both figures, I, II, and III indicate the series with the first TMA pulse introduced after a total number of DEZ+DI and MCp2Mg+DI pulses equal to 24, 96, and 384, respectively. The Mg content in the samples series shown here varied between (9.1 ± 0.3) and (9.9 ± 0.3) at. %.

Indeed, the extracted Φ_{bp}^{ZnO} and Φ_{bp}^{MgO} are in very good agreement with the values [(2.8 ± 0.1) and (3.9 ± 0.3) eV, respectively] obtained by Mönch in Ref. 23 on the basis of experimental data from ZnO- and MgO-based heterostructures to a wide variety of semiconductor counterparts. Moreover, for the holes Schottky barrier height, a value of ∼2.2 eV has been extracted from x-ray photoelectron spectroscopy (XPS) measurements in the case of metallic RuO_2 deposited *in situ* on ZnO.[79,80] The corresponding Φ_{bp}^{ZnO} is found equal to ∼2.8 eV applying the equivalent of Eq. (10) for Schottky contacts and using 5.4 Miedema-unit and 3.7 as Ru Miedema's electronegativity and ϵ_∞ for ZnO, respectively.[65,81] Furthermore, the Φ_{bp}^{ZnO} and Φ_{bp}^{MgO} extracted here, considering that, as mentioned above, the intrinsic dipole contribution can be neglected in the case of ZnO/MgO heterojunctions, anticipate ΔW_v in the ZnO/MgO junction case equal to ∼0.9 eV in agreement with the XPS measured value for such heterostructures.[82] This further supports our Φ_{bp}s estimates considering that XPS characterization is the reference technique for band-alignment studies. In addition, it justifies *a posteriori* the assumption of a linear Φ_{bp}^{ZnMgO} dependence over the whole x range, i.e., Equation (11). That is, the above-mentioned theoretical correction due to the change in crystal structure is essentially within our experimental uncertainty even though it might explain the ∼0.3 eV lower Φ_{bp}^{MgO} estimate extracted here with respect to the value found by Mönch. On the other hand, on the basis of the analysis of Schottky contacts to ZnO using different metals, Φ_{bp}^{ZnO} was placed (2.45 ± 0.05) eV above the valence band maximum.[83] This ∼0.25 eV difference with respect to the value obtained here is larger than the generally reported ∼0.1 eV Φ_{bp} fluctuation between values extracted from Schottky contacts and heterostructures[23] and requires further investigations. Overall, despite these fluctuations, it should be noted that the values of Φ_{bp}^{ZnO} and Φ_{bp}^{MgO} found here are ∼0.6–0.9 and ∼1.8 eV lower than the theoretical calculated ones for ZnO and MgO, respectively.[21–23]

In this context, it is also worth stressing that in the case of ZnO, these calculated estimates have been backed up by XPS measurements that are often extended to other material systems with established branch point energies by using the transitivity rule. This approach fails when the electronegativity contribution in Eq. (10) is significant. Furthermore, possible polarity or reaction effects are implicitly assumed to be negligible if the transitivity rule is used, even though this might not be the case especially when lattice matching substrates/high growth temperatures are used. As an example, an ∼0.67 eV difference in the ZnO/GaN valence band alignment is found if values originally extracted from ZnO/AlN and ZnO/Cu_2O heterostructures are used.[84,85]

C. Photovoltaic response of the realized structures

As mentioned in the Introduction, the focuses of the majority of the previous attempts to achieve high yield n-ZnO/p-Si based solar cells were the technological procedures, the characteristics of the films deposited, and the photovoltaic response of the devices realized. On the other hand, little attention was paid to the correlation between these parameters and ΔE_C. To fill this gap and provide a touchstone for further improvements of the performances, the electrically characterized n-ZnO/p-Si based heterostructures were also measured under STC conditions with the extracted active area short circuit currents (J_{SC}s), V_{OC}s, and ηs shown in Figs. 10(a) and 10(b), and in the inset of (b), respectively (for a full overview of the collected data from which they are extracted, see Fig. S7 in the supplementary material). The photovoltaic response of the devices based on $Zn_{(1-x)}Mg_xO$ layers as well as ΔE_C was found to be close to what has been previously reported in the case of samples realized similarly but using different growth parameters for the emitter.[20] Furthermore, J_{SC} was observed to vary in the ∼33–28 mA/cm^2 range with no clear correlation with the Mg content [see Figs. 10(a), S7(f), and the corresponding caption for more details]. Similarly, no dependence on the Mg content was observed in the case of R_S and R_P that were found to oscillate in the ∼1–6 and $\gtrsim 500\,\Omega\,cm^2$ ranges, respectively (the values multiplied by the device active area were considered in the analysis of the photovoltaic response of the examined samples).[86] As evident from Fig. 10(b), the not intentionally doped samples presented the lowest V_{OC}s that were found to be ≲340 mV. Note that, as discussed in the previous Subsection, for these samples, the ΔE_C reported in Fig. 4 is the apparent one and E_{bb} should be added. This places ΔE_C at the same level as the $Zn_{0.94}Mg_{0.06}O$:Al one with the corresponding ∼40 mV larger V_{OC} observed in this case possibly indicating a slight underestimation of E_{bb}. A further comparison between Figs. 11(b) and 4 reveals that the observed ∼0.1 eV reduction of ΔE_C following the increasing Mg content from x ∼0.06 to ∼0.09 and from x ∼0.14 to ∼0.16 correlates with the ∼20 and ∼40 mV larger V_{OC}s measured, respectively. In addition, no significant changes in V_{OC} were observed for Mg contents ≳0.16 consistent with the extracted ΔE_C being constant in the ∼0.2–0.25 Mg interval. On the other hand, to the ∼20 mV V_{OC} increase occurring for x in the ∼0.09–0.14 range, a corresponding plateau in ΔE_C was found, even though the errors on ΔE_C can mask a possible reduction in this case. As mentioned in the Introduction, such dependence of J_{SC} and V_{OC} on ΔE_C is indeed expected. That is, overall the trends found are at least in qualitative agreement with what is expected with a detailed explanation of the possible minor discrepancies being behind the scope of the present work. However, the maximum achieved V_{OC}s (∼450 mV) and ηs (∼7.2%) are, as in the case of previous reports, far below the theoretically predicted ones.[18] To exclude possible geometrical effects and consolidate the found results, full photovoltaic devices were realized [for a front view see Fig. 11(a)] and their photovoltaic response tested. This part of the study was limited to test solar cells with $Zn_{0.8}Mg_{0.2}O$:Al layers since, on the basis of what is shown in Fig. 10 and discussed above, they are anticipated to be among the ones exhibiting the highest η. Furthermore, the $Zn_{0.8}Mg_{0.2}O$:Al layer was deposited at 280 and 300 °C since an improvement in the

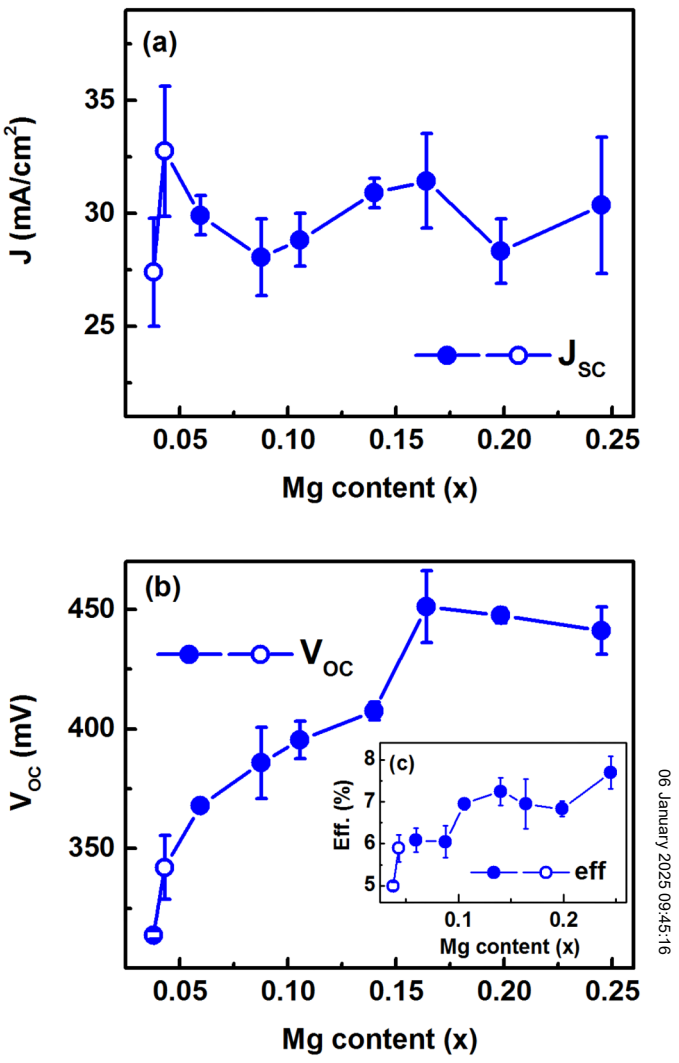

FIG. 10. (a) The active area J_{SC}s vs Mg content of the devices investigated. In (b) and the inset, the V_{OC} and η vs Mg content, respectively. In all graphs, empty circles are relative to layers where no Al was introduced.

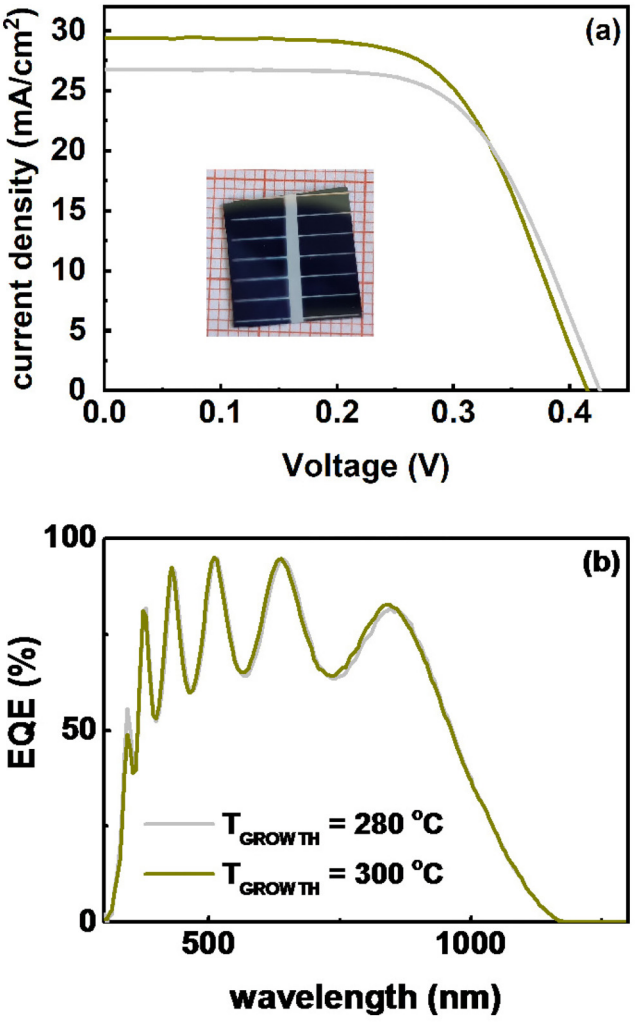

FIG. 11. (a) J–V characteristics under STC conditions with the current density (J) calculated using the active area of the device. In the same figure, a front view of one of the test solar cells is shown. In (b), the external quantum efficiency (EQE) response of the same samples is shown. A representative curve for a cell with the $Zn_{0.8}Mg_{0.2}O$:Al layer deposited at 280 and 300 °C is shown in both cases.

photovoltaic response by increasing the deposition temperature was reported in the previous published work.[20]

The J–V characteristics under STC conditions of two selected samples based on a $Zn_{0.8}Mg_{0.2}O$:Al layer are shown in Fig. 11(a). The J_{SC}s as extracted from the J–V characteristics shown were equal to (27.0 ± 0.3) and (29.1 ± 0.2) mA/cm^2 for the samples with the $Zn_{0.8}Mg_{0.2}O$:Al layer deposited at 280 and 300 °C, respectively. Here, it is worth pointing out that the latter value of J_{SC} is only ∼16% lower than ∼34 mA/cm^2, the theoretical expected value for such structures calculated using commercially available programs like OPAL and wafer ray-tracing.[87] This suggests that J_{SC}s similar to the ones reported for commercially available HJT are achievable for such structures if texturized substrates are used.[7] The corresponding EQE responses in the 300–1200 nm wavelength range are shown in Fig. 11(b). Interference peaks, consistent with the planar structure of the devices, were observed with the EQE oscillating between ∼60% and ∼95% within the 400–940 nm wavelength range. From these EQE spectra, since the spectral irradiance [$E(\lambda)$] is known, the photocurrent density (J_{SC}^{qe}) was evaluated according to

$$J_{SC}^{qe} = e\int_{\lambda_1}^{\lambda_2} EQE(\lambda)E(\lambda)\,d\lambda, \tag{12}$$

with λ_1 and λ_2 being equal to the EQE spectrum limiting wavelengths that are 300 and 1400 nm, respectively.

Using for $E(\lambda)$ the AM1.5 global spectrum ASTM G-173-03 with an integrated power of 1000 W/m^2 corresponding to the illumination conditions, J_{SC}^{qe} was found equal to (29.0 ± 0.1) mA/cm^2 in both cases. The substantial agreement between J_{SC}s and J_{SC}^{qe}s not only confirms the high J_{SC}s found here and in similar structures[20] but also excludes a significant contribution from micro-shunts that act as a shunting load if the cell is irradiated only on a limited area as in the case of EQE measurements.[66] Within the analyzed samples, the V_{OC}, fill factor (*FF*), and ηs were observed to vary in the (430 ± 20) mV, (61 ± 2)%, and (7.2 ± 0.3)%, respectively. On the other hand, R_S and R_P were found equal to (3 ± 1) and ≳1000 Ω cm^2. That is, the realized solar cells exhibited a photovoltaic response similar to the test devices. In addition, no significant differences were found between the samples with the $Zn_{0.8}Mg_{0.2}O$:Al layer deposited at 280 and at 300 °C. This finding is indeed consistent with the similar XRD patterns measured (as shown in Fig. S8 in the supplementary material) in the two cases indicating the absence of detectable structural changes differently to what is occurring when lower deposition temperatures are used.[20] Finally, overall, the photovoltaic response of the test solar cells were found to be stable after 7-month storage in air at RT. With respect to previously reported characteristics of structures realized with a similar procedure, the present ones exhibited similar J_{SC}s but a ∼100 mV larger V_{OC},[20] thus representing a considerable improvement. Here, it is worth pointing out that, as mentioned in the Introduction, even though higher values of V_{OC} up to ∼540 mV have been reported, overall, these values are anyhow well below the ∼620–660 mV range indicated by theoretical simulations or the highest V_{OC}s achieved in the case of HJTs solar cells that are in the ∼0.71–0.75 V range.[7] The same holds for the *FF* that is reported to be ≳10% lower than the expected one.[16,18,19] In our case, as shown in Fig. 4, the measured ΔE_C is (0.61 ± 0.02) eV for Mg contents varying in the (0.2–0.24) range with the conduction band lowering contribution due to the many body effects being (0.31 ± 0.02) eV, that is, accounting for ∼50% of the total. Hence, lower than simulated, V_{OC} as well as *FF* are indeed anticipated.[18] In this respect, however, it is worth noticing that the relatively high R_Ss of the realized test solar cells contribute significantly in reducing the latter as well.[88] Furthermore, the fact that, as mentioned above, considerably lower V_{OC} and *FF* are experimentally obtained even for devices that are optimized for photovoltaic purposes suggests that, also in these

cases, a staggered type II band alignment was among the main factors limiting the obtained ηs that have been reported to be $\geq$10% lower than in the HJTs solar cells case.[7,16] Finally, here it is worth pointing out that the ΔE_C^0 value for the n-ZnO/SiO_x/p-Si heterostructures of (0.69 ± 0.03) eV as well as the ΔE_C^0 reduction vs increasing Mg content of (1.7 ± 0.2) eV extracted here are considerably different with respect to the ones used in the previously published simulations that were set to 0.3 and 2.7 eV, respectively.[18] Thus, while the trends are preserved, the absolute values extracted from the simulations are overestimates for a specific Mg content and the theoretically calculated V_{OC} as well as η represent indeed upper limits, unless further mechanisms for reducing the conduction band misalignment between the ZnO-based layer and the Si substrate are found.

IV. CONCLUSIONS

In this work, a detailed study of the conduction band alignment between nominally undoped and Al-doped $Zn_{(1-x)}Mg_xO$ layers and (100) p-Si in the presence of native SiO_x has been presented. Considering that even the nominally undoped $Zn_{(1-x)}Mg_xO$ layers were degenerate and carrier concentration up to 4×10^{20} cm^{-3} could be achieved by introducing Al while keeping the Mg content $x < 0.16$ conduction band lowering due to the many body effects was anticipated to have a significant impact on ΔE_C. By correcting the measured ΔE_C for this contribution taking into account the conduction band non-parabolicity of ZnO, the expected linear increase of ΔE_C vs Mg content was recovered with the extracted proportionality factor being equal to (1.7 ± 0.2) eV. From this dependence on the $Zn_{(1-x)}Mg_xO$:Al layers composition considering the presence of the SiO_x interlayer that accounts for 20% of the bands' misalignments, and under the assumption of a linear variation between the respective values of the corresponding two binary compound semiconductors, ZnO and MgO, branch point energies for ZnO and MgO equal to (2.7 ± 0.2) and (3.6 ± 0.4) eV were extracted, respectively. Full 1×1 cm test solar cells based on $Zn_{0.8}Mg_{0.2}O$:Al layers exhibited short circuit currents, open circuit voltages, fill factors, and efficiencies fluctuating in the (28 ± 1) mA/cm^2, (430 ± 20) mV, (61 ± 2)%, and (7.2 ± 0.3)% ranges independent of the growth temperature that was varied in the 280–300 °C range. Besides further optimization of this kind of structures, the present study evidences that, even with ~12 at. % Mg content, the residual ΔE_C ~0.61 eV can be reduced only down to ~0.30 eV by decreasing the carrier concentration in the $Zn_{(1-x)}Mg_xO$:Al layer, that is, by minimizing the conduction band lowering due to the many body effects and the electron–donor interaction. Furthermore, increasing the Mg content up to x ~0.35, the maximum Mg content reported for the $Zn_{(1-x)}Mg_xO$ wurtzite phase would result still in a type II band alignment with $\Delta E_C \sim 0.11$ eV. Therefore, alternative routes should be investigated to further improve the photovoltaic performances of devices based on n – $Zn_{(1-x)}Mg_xO$:Al/SiO_x/p-Si.

SUPPLEMENTARY MATERIAL

See the supplementary material for additional experimental details: S1: The ratio of the Mg atomic content and the sum of the Zn, Mg, and Al atomic content vs the ratio between the Mg number of ALD cycles and the sum of the Zn, Mg, and Al ones. S2: HAADF STEM and EDS elemental mapping images of the $Zn_{0.84}Mg_{0.16}O$:Al and $Zn_{0.75}Mg_{0.25}O$:Al layers. S3: ABF and HAADF STEM images of the $Zn_{0.94}Mg_{0.06}O$:Al, $Zn_{0.84}Mg_{0.16}O$:Al, and $Zn_{0.75}Mg_{0.25}O$:Al layers. S4: Comparison between the SEM cross-sectional, top view images and XRD patterns of $Zn_{(1-x)}Mg_xO$ layers on Si with the same nominal Mg content with and without Al. S5: SEM cross-sectional, top view images of selected $Zn_{1-x}Mg_xO$:Al and XRD patterns of $Zn_{1-x}Mg_xO$:Al layers over the whole Mg interval investigated with and without Al. S6: SIMS profiles of $Zn_{(1-x)}Mg_xO$:Al layers where the first TMA pulse was introduced after a total number of DEZ+DI and MCp2Mg+DI pulses equal to 24, 96, and 384 (series I–III in the main text). S7: Complete overview of the photovoltaic response of the devices presenting the structure shown in the inset of Fig. 3(a) in the main text. S8: Comparison between the XRD patterns of $Zn_{0.8}Mg_{0.2}O$:Al layers deposited at 280 and 300 °C.

ACKNOWLEDGMENTS

The work was performed within the Polish National Science Centre (NCN) Project No. UMO-2016/22/E/ST3/00553.

AUTHOR DECLARATIONS

Conflict of Interest

The authors have no conflicts to disclose.

Author Contributions

R. Schifano: Conceptualization (lead); Data curation (equal); Formal analysis (equal); Funding acquisition (lead); Investigation (equal); Methodology (lead); Project administration (lead); Resources (lead); Software (equal); Supervision (lead); Validation (lead); Visualization (lead); Writing – original draft (lead). **S. Gieraltowska:** Conceptualization (equal); Data curation (equal); Investigation (equal); Methodology (equal); Validation (equal); Writing – review & editing (equal). **J. Kurek:** Conceptualization (equal); Data curation (equal); Formal analysis (equal); Investigation (equal); Methodology (equal); Visualization (equal); Writing – review & editing (equal). **L. Wachnicki:** Investigation (equal); Writing – review & editing (equal). **U. Rehman:** Conceptualization (equal); Data curation (equal); Formal analysis (equal); Investigation (equal); Validation (equal); Writing – review & editing (equal). **D. Budiakivska:** Data curation (equal); Formal analysis (equal); Investigation (equal); Validation (equal); Visualization (equal); Writing – review & editing (equal). **S. Chusnutdinow:** Conceptualization (equal); Formal analysis (equal); Investigation (equal); Resources (equal); Validation (equal); Writing – review & editing (equal). **K. Kopalko:** Conceptualization (equal); Investigation (equal); Writing – review & editing (equal). **R. Jakiela:** Conceptualization (equal); Formal analysis (equal); Investigation (equal); Resources (equal); Validation (equal); Visualization (equal); Writing – review & editing (equal). **S. Porro:** Conceptualization (equal); Investigation (equal); Methodology (equal); Resources (equal); Validation (equal); Writing – review & editing (equal). **R. Minikayev:**

Conceptualization (equal); Formal analysis (equal); Investigation (equal); Resources (equal); Validation (equal); Visualization (equal); Writing – review & editing (equal). **B. S. Witkowski:** Formal analysis (equal); Investigation (equal); Resources (equal); Writing – review & editing (equal). **M. Pawlowski:** Investigation (equal); Resources (equal); Software (equal); Supervision (equal); Writing – review & editing (equal). **C. Jastrzebski:** Investigation (equal); Resources (equal); Supervision (equal); Validation (equal); Writing – review & editing (equal). **A. Thøgersen:** Conceptualization (equal); Data curation (equal); Formal analysis (equal); Funding acquisition (equal); Investigation (equal); Methodology (equal); Resources (equal); Software (equal); Validation (equal); Visualization (equal); Writing – review & editing (equal).

DATA AVAILABILITY

The data that support the findings of this study are available within the article and its supplementary material.

REFERENCES

[1]H. Kobayashi, Y. Kogetsu, T. Ishida, and Y. Nakato, "Increases in photovoltage of 'indium tin oxide/silicon oxide/mat-textured n-silicon' junction solar cells by silicon preoxidation and annealing processes," J. Appl. Phys. **74**, 4756–4761 (1993).

[2]H. Kobayashi, T. Ishida, Y. Nakato, and H. Tsubomura, "Mechanism of carrier transport in highly efficient solar cells having indium tin oxide/Si junctions," J. Appl. Phys. **69**, 1736–1743 (1991).

[3]J. Shewchun, D. Burk, and M. B. Spitzer, "MIS and SIS solar cells," IEEE Trans. Electron Devices **27**, 705–716 (1980).

[4]*Transparent Conductive Zinc Oxide*, edited by K. Ellmer, A. Klein, and B. Rech, Springer Series in Materials Science (Springer, Berlin, 2008), Vol. 104.

[5]*Zinc Oxide Bulk, Thin Films and Nanostructures*, edited by C. Jagadish and S. J. Pearton (Elsevier Ltd, Oxford, 2006).

[6]A. Razzaq, T. G. Allen, W. Liu, Z. Liu, and S. De Wolf, "Silicon heterojunction solar cells: Techno-economic assessment and opportunities," Joule **6**, 514–542 (2022).

[7]M. A. Green, E. D. Dunlop, M. Yoshita, N. Kopidakis, K. Bothe, G. Siefer, and X. Hao, "Solar cell efficiency tables (version 63)," Prog. Photovolt. **32**, 3–13 (2024).

[8]N. M. Haegel *et al.*, "Photovoltaics at multi-terawatt scale: Waiting is not an option," Science **380**, 39–42 (2023).

[9]G. G. Untila, T. N. Kost, and A. B. Chebotareva, "Bifacial 8.3%/5.4% front/rear efficiency ZnO:Al/n-Si heterojunction solar cell produced by spray pyrolysis," Sol. Energy **127**, 184–197 (2016).

[10]D. G. Baik and S. M. Cho, "Application of sol-gel derived films for ZnO/n-Si junction solar cells," Thin Solid Films **354**, 227–231 (1999).

[11]L. Shen, Z. Q. Ma, C. Shen, F. Li, B. He, and F. Xu, "Studies on fabrication and characterization of a ZnO/p-Si-based solar cell," Superlatt. Microstruct. **48**, 426–433 (2010).

[12]A. A. Ibrahim and A. Ashour, "ZnO/Si solar cell fabricated by spray pyrolysis technique," J. Mater. Sci.: Mater. Electron. **17**, 835–839 (2006).

[13]R. Pietruszka, G. Luka, B. S. Witkowski, K. Kopalko, E. E. Zielony, P. Bieganski, E. Placzek-Popko, and M. Godlewski, "Electrical and photovoltaic properties of ZnO/Si heterostructures with ZnO films grown by atomic layer deposition," Thin Solid Films **563**, 28–31 (2014).

[14]R. Pietruszka, B. S. Witkowski, E. E. Zielony, E. Placzek-Popko, and M. Godlewski, "ZnO/Si heterojunction solar cell fabricated by atomic layer deposition and hydrothermal methods," Sol. Energy **155**, 1282–1288 (2017).

[15]O. Bethge, M. Nobile, S. Abermann, M. Glaser, and E. Bertagnolli, "ALD grown bilayer junction of ZnO:Al and tunnel oxide barrier for SIS solar cell," Sol. Energy Mater. Sol. Cells **117**, 178–182 (2013).

[16]G. G. Untila, T. N. Kost, and A. B. Chebotareva, "Fluorine-doped ZnO (FZO) films produced by corona-discharge-assisted ultrasonic spray pyrolysis and hydrogenation as electron-selective contacts in FZO/SiO_x/p-Si heterojunction crystalline silicon solar cells with 11.7% efficiency," Sol. Energy **179**, 352–362 (2019).

[17]F.-H. Hsu, N.-F. Wang, Y.-Z. Tsai, and M.-P. Houng, "A novel Al and Y codoped ZnO/n-Si heterojunction solar cells fabricated by pulsed laser deposition," Sol. Energy **86**, 3146–3152 (2012).

[18]K. E. Knutsen, R. Schifano, E. S. Marstein, B. G. Svensson, and A. Y. Kuznetsov, "Prediction of high efficiency ZnMgO/Si solar cells suppressing carrier recombination by conduction band engineering," Phys. Status Solidi A **210**, 585–588 (2013).

[19]B. Hussain, A. Ebong, and I. Ferguson, "Zinc oxide as an active n-layer and antireflection coating for silicon based heterojunction solar cell," Sol. Energy Mater. Sol. Cells **139**, 95–100 (2015).

[20]R. Pietruszka, R. Schifano, T. A. Krajewski, B. S. Witkowski, K. Kopalko, L. Wachnicki, E. Zielony, K. Gwozdz, P. Bieganski, E. Placzek-Popko, and M. Godlewski, "Improved efficiency of n-ZnO/p-Si based photovoltaic cells by band offset engineering," Sol. Energy Mater. Sol. Cells **147**, 164–170 (2016).

[21]A. Schleife, F. Fuchs, C. Rödl, J. Furthmüller, and F. Bechstedt, "Branch-point energies and band discontinuities of III-nitrides and III-/II-oxides from quasiparticle band-structure calculations," Appl. Phys. Lett. **94**, 012104 (2009).

[22]J. Robertson and B. Falabretti, "Band offsets of high K gate oxides on III-V semiconductors," J. Appl. Phys. **100**, 014111 (2006).

[23]W. Mönch, "Branch-point energies and the band-structure lineup at Schottky contacts and heterostructures," J. Appl. Phys. **109**, 113724 (2011).

[24]G. Luka, T. A. Krajewski, B. S. Witkowski, G. Wisz, I. S. Virt, E. Guziewicz, and M. Godlewski, "Aluminum-doped zinc oxide films grown by atomic layer deposition for transparent electrode applications," J. Mater. Sci.: Mater. Electron. **22**, 1810–1815 (2011).

[25]R. Schifano, P. Dluzewski, W. Zajkowska, B. Kurowska, T. A. Krajewski, R. Jakiela, G. Luka, B. S. Witkowski, D. Jarosz, R. Minikayev, A. Wierzbicka, K. Goscinski, K. Kopalko, E. Guziewicz, and P. S. Smertenko, "Schottky contacts to ZnO layers grown by atomic layer deposition: Effects of H_2O_2 functionalization and transport mechanisms," Appl. Surf. Sci. **552**, 149067 (2021).

[26]R. Chwang, B. J. Smith, and C. R. Crowell, "Contact size effects on the van der Pauw method for resistivity and Hall coefficient measurement," Solid State Electron. **17**, 1217–1227 (1974).

[27]T. Zdanowicz and D. Tomczak, "IV curve fitter v.1.8 ©software, 2002," in *5th IEEE Photovoltaic Specialists Conference* (IEEE, Honolulu, 2010), pp. 2184–2187, http://www.pvmeasurement.com/index.php.

[28]G. Luka, B. S. Witkowski, L. Wachnicki, K. Goscinski, R. Jakiela, E. Guziewicz, M. Godlewski, E. Zielony, P. Bieganski, E. Placzek-Popko, W. Lisowski, J. W. Sobczak, and A. Jablonski, "Atomic layer deposition of $Zn_{1-x}Mg_x$O:Al transparent conducting films," J. Mater. Sci.: Mater. Electron. **49**, 1512–1518 (2014).

[29]J. G. Lu, S. Fujita, T. Kawaharamura, H. Nishinaka, Y. Kamada, and T. Ohshima, "Carrier concentration induced band-gap shift in Al-doped $Zn_{1-x}Mg_x$O thin films," Appl. Phys. Lett. **89**, 262107 (2006).

[30]D. J. Cohen, K. C. Ruthe, and S. A. Barnett, "Transparent conducting $Zn_{1-x}Mg_x$O:(Al,In) thin films," J. Appl. Phys. **96**, 459–467 (2004).

[31]A. Mošková, M. Moško, M. Precner, M. Mikolášek, A. Rosová, M. Mičušík, V. Štrbík, J. Šoltýs, F. Gucmann, E. Dobročka, and K. Fröhlich, "Doping efficiency and electron transport in Al-doped ZnO films grown by atomic layer deposition," J. Appl. Phys. **130**, 035106 (2021).

[32]Since there is experimental evidence that only ∼10%–20% of Al acts as a donor, i.e., it is incorporated in the Zn lattice sites, the expression $Zn_{(1-x)}Mg_x$O:Al has been preferred to $Zn_{(1-x-y)}Mg_xAl_y$O thorough the presented work.

[33]Y. Wu, A. D. Giddings, M. A. Verheijen, B. Macco, T. J. Prosa, D. J. Larson, F. Roozeboom, and W. M. M. Kessels, "Dopant distribution in atomic layer

deposited ZnO:Al films visualized by transmission electron microscopy and atom probe tomography," Chem. Mater. **30**, 1209–1217 (2018).
[34]A. Yanguas-Gil, K. E. Peterson, and J. W. Elam, "Controlled dopant distribution and higher doping efficiencies by surface-functionalized atomic layer deposition," Chem. Mater. **23**, 4295–4297 (2011).
[35]R. L. Puurunen, "Surface chemistry of atomic layer deposition: A case study for the trimethylaluminum/water process," J. Appl. Phys. **97**, 121301 (2005).
[36]T. Tynell and M. Karppinen, "Atomic layer deposition of ZnO: A review," Semicond. Sci. Technol. **29**, 043001 (2014).
[37]A. Bikowski, M. Rengachari, M. Nie, N. Wanderka, P. Stender, G. Schmitz, and K. Ellmer, "Research update: Inhomogeneous aluminium dopant distribution in magnetron sputtered ZnO:Al thin films and its influence on their electrical properties," APL Mater. **3**, 060701 (2015).
[38]J. Stehr, K. Johansen, T. Bjørheim, L. Vines, B. Svensson, W. Chen, and I. Buyanova, "Zinc-vacancy–donor complex: A crucial compensating acceptor in ZnO," Phys. Rev. Appl. **2**, 021001 (2014).
[39]J.-Y. Noh, H. Kim, Y.-S. Kim, and C. H. Park, "Electron doping limit in Al-doped ZnO by donor-acceptor interactions," J. Appl. Phys. **113**, 153703 (2013).
[40]Y. Ke, S. Lany, J. J. Berry, J. D. Perkins, P. A. Parilla, A. Zakutayev, T. Ohno, R. O'Hayre, and D. S. Ginley, "Enhanced electron mobility due to dopant-defect pairing in conductive ZnMgO," Adv. Funct. Mater. **24**, 2875–2882 (2014).
[41]*Heterojunctions Band Discontinuities*, edited by F. Capasso and G. Margaritondo (Elsevier, Amsterdam, 1987).
[42]M. Guziewicz, R. Schifano, E. Przezdziecka, J. Z. Domagala, T. A. Jung, W. Krajewski, and E. Guziewicz, "n-ZnO/p-4H-SiC diode: Structural, electrical, and photoresponse characteristics," Appl. Phys. Lett. **107**, 101105 (2015).
[43]J. H. Werner, "Schottky barrier and pn-junction I/V plots - small signal evaluation," Appl. Phys. A **47**, 291–300 (1988).
[44]*The Electrical Characterization of Semiconductors: Majority Carriers and Electron States*, edited by P. Blood and J. W. Orton (Academic Press, London, 1992).
[45]B. Brar, G. D. Wilk, and A. C. Seabaugh, "Direct extraction of the electron tunneling effective mass in ultrathin SiO_2," Appl. Phys. Lett. **69**, 2728–2730 (1996).
[46]*Metal-Semiconductor Contacts*, edited by E. H. Rhoderick and R. H. Williams (Oxford University Press, Clarendon Press, Oxford, 1988).
[47]A. M. Cowley, "Depletion capacitance and diffusion potential of gallium phosphide Schottky barrier diodes," J. Appl. Phys. **37**, 3024 (1966).
[48]W. Lu, C. Leendertz, L. Korte, J. A. Töfflinger, and H. Angermann, "Passivation properties of subnanometer thin interfacial silicon oxide films," Energy Procedia **55**, 805–812 (2014).
[49]M. A. Green, "Intrinsic concentration, effective densities of states, and effective mass in silicon," J. Appl. Phys. **67**, 2944–2954 (1990).
[50]M. Heinemann and C. Heiliger, "Auger recombination rates in ZnMgO from first principles," J. Appl. Phys. **110**, 083103 (2011).
[51]C. Franz, M. Giar, M. Heinemann, M. Czerner, and C. Heiliger, "Band structure and effective masses of $Zn_{1-x}Mg_xO$," MRS Online Proc. Lib **1494**, 57–63 (2013).
[52]T. Pisarkiewicz and A. Kolodziej, "Nonparabolicity of the conduction band structure in degenerate tin dioxide," Phys. Status Solidi B **158**, K5–K8 (1990).
[53]W. M. Kim, I. H. Kim, J. H. Ko, B. Cheong, T. S. Lee, K. S. Lee, D. Kim, and T. Y. Seong, "Density-of-state effective mass and non-parabolicity parameter of impurity doped ZnO thin films," J. Phys. D: Appl. Phys. **41**, 195409 (2008).
[54]R. Schifano, R. Jakiela, A. Galeckas, K. Kopalko, F. Herklotz, K. M. H. Johansen, and L. Vines, "Role of intrinsic and extrinsic defects in H implanted hydrothermally grown ZnO," J. Appl. Phys. **126**, 125707 (2019).
[55]J. A. Sans, J. F. Sánchez-Royo, A. Segura, G. Tobias, and E. Canadell, "Chemical effects on the optical band-gap of heavily doped ZnO:M_{III} (M = Al, Ga,In): An investigation by means of photoelectron spectroscopy, optical measurements under pressure, and band structure calculations," Phys. Rev. B **79**, 195105 (2009).
[56]J. C. Inkson, "The effect of electron interaction on the band gap of extrinsic semiconductors," J. Phys. C: Solid State Phys. **9**, 1177–1183 (1976).
[57]K. F. Berggren and B. E. Sernelius, "Band-gap narrowing in heavily doped many-valley semiconductors," Phys. Rev. B **24**, 1971–1986 (1981).
[58]B. E. Sernelius, "Self-energy shifts in heavily doped, polar semiconductors," Phys. Rev. B **36**, 4878–4887 (1987).
[59]R. A. Abram, G. N. Childs, and P. A. Saunderson, "Band gap narrowing due to many-body effects in silicon and gallium arsenide," J. Phys. C: Solid State Phys. **17**, 6105–6125 (1984).
[60]S. C. Jain and D. J. Roulston, "A simple expression for band gap narrowing (BGN) in heavily doped Si, Ge, GaAs and Ge_xSi_{1-x} strained layers," Solid State Electron. **34**, 453–465 (1991).
[61]S. C. Jain, J. M. McGregor, and D. J. Roulston, "Band gap narrowing in novel III-V semiconductors," J. Appl. Phys. **68**, 3747–3749 (1990).
[62]In Ref. 59, the wave vector dependence of the plasmon angular frequency up to the power of four was included. In the present work, the expression limited to the quadratic term is used following the original work of Inkson (Refs. 56 and 57).
[63]Y. Wang, W. Tang, L. Zhang, and J. Zhao, "Electron concentration dependence of optical band gap shift in Ga-doped ZnO thin films by magnetron sputtering," Thin Solid Films **565**, 62–68 (2014).
[64]M. Feneberg, J. Nixdorf, C. Lidig, R. Goldhahn, Z. Galazka, O. Bierwagen, and J. S. Speck, "Many-electron effects on the dielectric function of cubic In_2O_3: Effective electron mass, band nonparabolicity, band gap renormalization, and Burstein-Moss shift," Phys. Rev. B **93**, 045203 (2016).
[65]*Electronic Properties of Semiconductor Interfaces*, edited by W. Mönch (Springer-Verlag, Berlin, Heidelberg, 2004).
[66]*Chalcogenide Photovoltaics*, edited by R. Scheer and H.-W. Schock (Wiley-VCH Verlag & Co. KGaA, Weinheim, Germany, 2011).
[67]W. Mönch, "On the alleviation of Fermi-level pinning by ultrathin insulator layers in Schottky contacts," J. Appl. Phys. **111**, 073706 (2012).
[68]J. Tersoff, "Schottky barrier heights and the continuum of gap states," Phys. Rev. Lett. **52**, 465 (1984).
[69]R. P. Howson and A. Taylor, "The optical properties of evaporated silicon oxide films," Thin Solid Films **9**, 109–119 (1972).
[70]W. Mönch, "On the electric-dipole contribution to the valence-band offsets in semiconductor-oxide heterostructures," Appl. Phys. Lett. **91**, 042117 (2007).
[71]C. Choopun, R. D. Vispute, W. Yang, R. P. Sharma, T. Venkatesan, and H. Shen, "Realization of band gap above 5.0 eV in metastable cubic-phase $Mg_xZn_{1-x}O$ alloy films," Appl. Phys. Lett. **80**, 1529–1531 (2002).
[72]A. Schleife, C. Rödl, J. Furthmüller, and F. Bechstedt, "Electronic and optical properties of $Mg_xZn_{1-x}O$ and $Cd_xZn_{1-x}O$ from *ab initio* calculations," New J. Phys. **13**, 085012 (2011).
[73]A. Ohtomo, M. Kawasaki, T. Koida, K. Masubuchi, H. Koinuma, Y. Sakurai, Y. Yoshida, T. Yasuda, and Y. Segawa, "$Mg_xZn_{1-x}O$ as a II–VI widegap semiconductor alloy," Appl. Phys. Lett. **72**, 2466–2468 (1998).
[74]G. Luka, L. Wachnicki, B. Witkowski, T. Krajewski, R. Jakiela, E. Guziewicz, and M. Godlewski, "The uniformity of Al distribution in aluminum-doped zinc oxide films grown by atomic layer deposition," Mater. Sci. Eng. B **176**, 237–241 (2011).
[75]W. Shan, W. Walukiewicz, J. W. Ager, K. M. Yu, Y. Zhang, S. S. Mao, R. Kling, C. Kirchner, and A. Waag, "Pressure-dependent photoluminescence study of ZnO nanowires," Appl. Phys. Lett. **86**, 153117 (2005).
[76]R. Jaramillo, A. Youssef, A. Akey, F. Schoofs, S. Ramanathan, and T. Buonassisi, "Using atom-probe tomography to understand ZnO:Al/SiO_2/Si Schottky diodes," Phys. Rev. Appl. **6**, 034016 (2016).
[77]At first sight, samples II and III do not fulfill the above discussed criteria of N_d uniformity necessary for extracting the actual ΔE_C. However, the $Zn_{(1-x)}Mg_xO$ is anticipated to be highly resistive and, in the first approximation, the analysis holds for Debye lengths of the order of the interlayer thickness (that is, for $n \lesssim 5 \times 10^{15}\,\mathrm{cm}^{-3}$ in the $Zn_{(1-x)}Mg_xO$ part of the layers). The same applies to Hall measurements.
[78]A positive effective charge equal to $\sim 2 \times 10^{11}\,\mathrm{cm}^{-2}$ has been reported to be present in the native SiO_x.[48]
[79]S. Li *et al.*, "Intrinsic energy band alignment of functional oxides," Phys. Status Solidi RRL **8**, 571–576 (2014).

[80]A. Klein, "Energy band alignment at interfaces of semiconducting oxides: A review of experimental determination using photoelectron spectroscopy and comparison with theoretical predictions by the electron affinity rule, charge neutrality levels, and the common anion rule," Thin Solid Films **520**, 3721–3728 (2012).
[81]Ü. Özgür, Y. I. Alivov, C. Liu, A. Teke, M. A. Reshchikov, S. Doğan, V. Avrutin, S.-J. Cho, and H. Morkoç, "A comprehensive review of ZnO materials and devices," J. Appl. Phys. **98**, 041301 (2005).
[82]Y. F. Li, B. Yao, Y. M. Lu, B. H. Li, Y. Q. Gai, C. X. Cong, Z. Z. Zhang, D. X. Zhao, J. Y. Zhang, D. Z. Shen, and X. W. Fan, "Valence-band offset of epitaxial ZnO/MgO (111) heterojunction determined by x-ray photoelectron spectroscopy," Appl. Phys. Lett. **92**, 192116 (2008).
[83]M. W. Allen and S. M. Durbin, "Role of a universal branch-point energy at ZnO interfaces," Phys. Rev. B **82**, 165310 (2010).
[84]T. D. Veal, P. D. C. King, S. A. Hatfield, L. R. Bailey, C. F. McConville, B. Martel, J. C. Moreno, E. Frayssinet, F. Semond, and J. Zúñiga-Pérez, "Valence band offset of the ZnO/AlN heterojunction determined by x-ray photoemission spectroscopy," Appl. Phys. Lett. **93**, 202108 (2008).
[85]B. Kramm, A. Laufer, D. Reppin, A. Kronenberger, P. Hering, A. Polity, and B. K. Meyer, "The band alignment of Cu_2O/ZnO and Cu_2O/GaN heterostructures," Appl. Phys. Lett. **100**, 094102 (2012).
[86]Note that corrections to J_{SC} and V_{OC} related to the presence of R_S and R_P within the observed ranges of these two quantities are negligible.
[87]S. C. Baker-Finc and K. R. McIntosh, "A freeware program for precise optical analysis of the front surface of a solar cell," in *Proceedings of the 12th European Photovoltaic Solar Energy Conference, 1994* (IEEE, 2010), pp. 1311–1314, https://www.pvlighthouse.com.au/.
[88]As an example in the case of the sample deposited at 300 °C corresponding to the J–V characteristic displayed in Fig. 11(a), simulations indicate that *FF* increases from ∼61% to ∼77% with η correspondingly rising from ∼7.5% up to ∼9.4% if R_S is reduced from ∼3 to 0.4 Ω cm^2. Such a reduction could be achieved, at least partly, by using a thinner $Zn_{0.8}Mg_{0.2}O$:Al layer while increasing the AZO thickness.